NTNU

Norwegian University of
Science and Technology

Modelling of Rotating Turbulent Flows
Computer simulation of turbulent backward-facing step flow with system rotation

Ted Ørjan Kjellevik Gundersen

Master of Science in Product Design and Manufacturing
Submission date: July 2011
Supervisor: Helge Ingolf Andersson, EPT
Co-supervisor: Mustafa Barri, EPT

Norwegian University of Science and Technology
Department of Energy and Process Engineering

NTNU

Norwegian University
of Science and Technology

Department of Energy
and Process Engineering

EPT-M-2011-65

MASTER THESIS

for

Stud.techn. Ted Ørjan K. Gundersen
Spring 2011

Computer simulation of turbulent backward-facing step flow with system rotation

Numerisk beregning av turbulent strømning i roterende kanal med plutselig tverrsnitt utvidelse

Background and objective.

Computational fluid dynamics (CFD) is a valuable tool in almost all industrial flow analysis and design. The reliability of CFD predictions depends on a number of different factors among which the physical complexity of the flow problem and the actual treatment of the turbulence are of major importance. The purpose of this project is to explore how different levels of turbulence modelling tackle the effects of system rotation on a massively separated turbulent flow. Commercial CFD-software, e.g. FLUENT, shall be used.

The following questions should be considered in the project work:

1 The candiate shall provide an overview of how different classes of turbulence models respond to Coriolis-force effects on the basis of available literature.
2 Two-dimensional Reynolds-averaged Navier-Stokes (RANS) calculations of turbulent flow over a backward-facing step shall be performed with a carefully selected turbulence model at some different rotation rates. The response to the system rotation shall be discussed.
3 An alternative turbulence model shall be chosen and the previous task repeated at one specific rate of rotation. The results obtained with the two different turbulence models shall be compared.
4 Comparisons with available data from laboratory and computer experiments (DNS) should be made and the correspondence between the calculations and the data commented on.
5 The candiate is expected to discuss the major advantages and disadvantges of the RANS-approach versus large-eddy simulations (LES) for this kind of flow problems.
6 The findings of the calculations are to be analysed and recommendations given for further advancements in the field.

-- " --

Within 14 days of receiving the written text on the master thesis, the candidate shall submit a research plan for his project to the department.

When the thesis is evaluated, emphasis is put on processing of the results, and that they are presented in tabular and/or graphic form in a clear manner, and that they are analyzed carefully.

The thesis should be formulated as a research report with summary both in English and Norwegian, conclusion, literature references, table of contents etc. During the preparation of the text, the candidate should make an effort to produce a well-structured and easily readable report. In order to ease the evaluation of the thesis, it is important that the cross-references are correct. In the making of the report, strong emphasis should be placed on both a thorough discussion of the results and an orderly presentation.

The candidate is requested to initiate and keep close contact with his/her academic supervisor(s) throughout the working period. The candidate must follow the rules and regulations of NTNU as well as passive directions given by the Department of Energy and Process Engineering.

Pursuant to "Regulations concerning the supplementary provisions to the technology study program/Master of Science" at NTNU §20, the Department reserves the permission to utilize all the results and data for teaching and research purposes as well as in future publications.
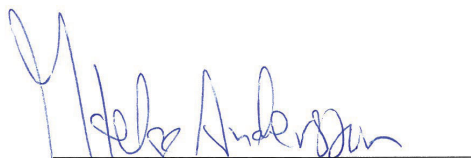
One – 1 complete original of the thesis shall be submitted to the authority that handed out the set subject. (A short summary including the author's name and the title of the thesis should also be submitted, for use as reference in journals (max. 1 page with double spacing)).
Two – 2 – copies of the thesis shall be submitted to the Department. Upon request, additional copies shall be submitted directly to research advisors/companies. A CD-ROM (Word format or corresponding) containing the thesis, and including the short summary, must also be submitted to the Department of Energy and Process Engineering

Department of Energy and Process Engineering, 17. January 2011

Olav Bolland
Department Head

Helge Andersson
Academic Supervisor

Research Advisor: Mustafa Barri (PhD)

Preface

This master thesis was written during the spring of 2011 and concludes my years as a student at NTNU. During my work with the thesis, I have deepened my knowledge within the field of computational fluid dynamics and specifically modelling of turbulent flows in rotating systems. An in-depth study of turbulence modelling is a complex task due to the advanced theory and the numerous approaches found in the literature. Although I have had my moments of frustration, the topic proved to be really exciting once I got the big picture.

I would like to thank my supervisor Professor Helge I. Andersson for helpful guidelines during my work with the thesis. In addition, I especially appreciate the opportunity to attend research seminars organised by Professor Andersson. My research advisor Dr Mustafa Barri also deserves special thanks for providing me with data for validation purposes. My fellow students Christopher Nilsen, Roy-Andre Midtgård and Lars Rypestøl should also be mentioned due to our useful discussions and pleasant lunch breaks.

Ted Ørjan Kjellevik Gundersen

II

Abstract

An investigation of how different levels of turbulence modelling tackle the effects of system rotation has been performed. Ranging from simple one-equation models to large-eddy simulations, different approaches have been considered by means of a literature study and numerical calculations of turbulent flow over a backward-facing step subjected to spanwise rotation. The computed results were compared with results from direct numerical simulations.

The literature study revealed that simple linear eddy-viscosity turbulence models are unable to predict any effects on the turbulence field due to system rotation. Eddy-viscosity models may be sensitised to rotation, but this has been done with a varying degree of success. The Reynolds stress equation models inherently respond well to system rotation, but a more costly eddy simulation will yield the most accurate result.

Numerical calculations confirmed what was found in the literature. A linear eddy-viscosity model was unaffected by system rotation, while the sensitised model exhibited some effects on the mean flow field. The Reynolds stress model managed to predict all essential effects related to system rotation, although one separation bubble was oversized. This defect was attributed to a flaw in the modelling of the Reynolds stress redistribution process.

IV

Sammendrag

Oppgavens formål er å undersøke hvordan ulike fremgangsmåter for turbulensmodellering med varierende kompleksitet reagerer på systemrotasjon. Alt fra enkle modeller med én transportligning til storevje-simuleringer har blitt undersøkt ved hjelp av et litteraturstudium og numeriske beregninger. Beregningene ble utført for turbulent strømning i en roterende kanal med plutselig tverrsnittsøkning. Resultatene har blitt sammenlignet med data fra direkte numeriske simuleringer.

I litteraturstudiet kom det frem at turbulensmodeller med en lineær sammenheng for turbulensviskositet ikke kan forutsi virkningen av systemrotasjon. Modeller basert på turbulensviskositet kan modifiseres slik at de påviser virkninger av rotasjon, men dette har blitt gjort med varierende resultater. Modeller basert på transportligningen til Reynolds-spenningene vil på grunn av deres opprinnelse i stor grad påvise effekter av systemrotasjon. Likevel vil en mer ressurskrevende storevje-simulering gi et mer presist resultat.

Numeriske beregninger bekreftet i stor grad resultatene fra litteraturstudiet. Løsningen gitt av en modell med lineær sammenheng for turbulensviskositet var uberørt av systemrotasjon, mens den modifiserte modellen påviste enkelte fenomen knyttet til systemrotasjon. En Reynolds-spenning-modell klarte å påvise alle de viktige effektene av systemrotasjon. Én resirkulasjonssone var likevel altfor stor, noe som ble tilskrevet en ufullkommen modellering av trykk-tøynings-leddet.

Contents

List of Figures

X

Chapter 1

Introduction

1.1 Background

Whether it be wind blowing in a storm or water flowing through pipes, most fluid flows found in nature and in engineering problems are turbulent. The complex turbulent state is well illustrated in a waterfall, where the structure of the flow is clearly chaotic. Predicting such a flow seems to be extremely difficult. Still, the equations describing the turbulent motions have been known for over a century. They are however too complex to be solved analytically. For many years, physical experiments were the only way of conducting research on these flows, which have been necessary in order to optimise efficiency and design in engineering problems.

As available computational resources increased, it became possible to solve the equations of fluid flow numerically. Computational fluid dynamics (CFD) has become very popular in the industry during the last few decades, mainly through the simplifying approach of turbulence modelling. CFD was first introduced in the aerospace industry, but have more recently spread to areas such as the motor vehicle industry and wind power assessment. The widespread popularity is due to the many advantages of CFD compared to experiments, as it is cheaper, applicable to otherwise impossible or dangerous scenarios and provides very detailed results. It is however important to bear in mind that CFD is not a substitute for experiments,

it is rather an additional problem solving tool. CFD results are at best as good as the underlying physics embedded in the code, and at worst as good as its operator. They need to be compared with experimental data from a similar setup in order to be validated. A skilled operator who can make the correct modelling choices and evaluate the results is therefore essential.

Rotating turbulent flows appear in both geophysical and engineering fluid mechanics. Earth's rotation affects the wind blowing in the atmosphere, as well as ocean currents. Turbomachinery products depend on system rotation as a part of their design concept. It is therefore important to understand how rotation affects turbulent flows in order to e.g. forecast the weather or design a pump.

1.2 Previous work

The present work has its foundation in a project work [19] by the author during the autumn of 2010. The project work provided an introduction to CFD through the commercial software ANSYS Fluent and Gambit. A grid study was conducted and several turbulence models were tested for the turbulent flow over a backward-facing step. Results were compared with DNS data from Barri *et al.* [7]. The project provided the author with important experience necessary in order to approach the current thesis in an efficient manner.

1.3 Purpose of the study

A wide range of CFD approaches have been presented throughout the years and many have been adopted by the industry and research community. Turbulence modelling is involved in most of them. Accuracy, efficiency and simplicity are the main criteria one strives for when a new approach is proposed. It is reasonable to assume that these criteria are related such that, in general, the simplest and most efficient methods yield the least accurate solutions. For rotating turbulent flows, this would imply that different approaches manage to account for the effects of rotation in a varying degree, depending on their complexity. The purpose of this study

is to explore how the different approaches involving turbulence modelling tackle the effects of system rotation. ANSYS Fluent will be used to perform some CFD calculations on a massively separated turbulent flow exposed to system rotation.

1.3.1 Outline of the report

Chapter 2 will cover theory relevant to the calculations in the present study. A short introduction to system rotation, turbulence modelling and other aspects of CFD is given. The mathematical formulation of the computational models used in the present study are given in detail. Additionally, basic theory for the large-eddy simulation (LES) approach is covered as a basis for parts of chapter 3.

Chapter 3 will provide an overview of how different CFD approaches involving turbulence modelling respond to system rotation. Approaches ranging from a simple one-equation model to the computationally costly LES will be covered and compared. Examples of relevant research conducted within the field will be reviewed and references given.

The flow case, turbulent flow over a backward-facing step subjected to spanwise rotation, will be introduced in chapter 4. The grid and boundary conditions used in the calculations will also be presented, along with a short text concerning the precursor calculations.

Results from the calculations will be presented in chapter 5. They are analysed and compared with data from Barri & Andersson [6]. Concluding remarks and suggestions for further work will subsequently be given in chapter 6.

Chapter 2

Theory

2.1   Fluid flow

Fluid flow can be described by equations based on conservation of mass, momentum and energy. We define the position vector $\boldsymbol{x} = (x, y, z)$ and the corresponding velocity vector $\boldsymbol{U} = (U, V, W)$. Then, for an incompressible Newtonian fluid, the continuity equation can be written, using Cartesian tensor notation, as

$$\frac{\partial U_i}{\partial x_i} = 0. \tag{2.1}$$

Neglecting the gravity force, the Navier–Stokes equations can similarly be written as

$$\frac{\partial U_i}{\partial t} + U_j \frac{\partial U_i}{\partial x_j} = -\frac{1}{\rho} \frac{\partial P}{\partial x_i} + \nu \frac{\partial^2 U_i}{\partial x_j \partial x_j} + \frac{F_i}{\rho}, \tag{2.2}$$

where ρ is the density, P is the pressure and ν is the kinematic viscosity of the fluid. F_i is external body forces acting on the fluid particle, e.g. centrifugal forces and the Coriolis force.
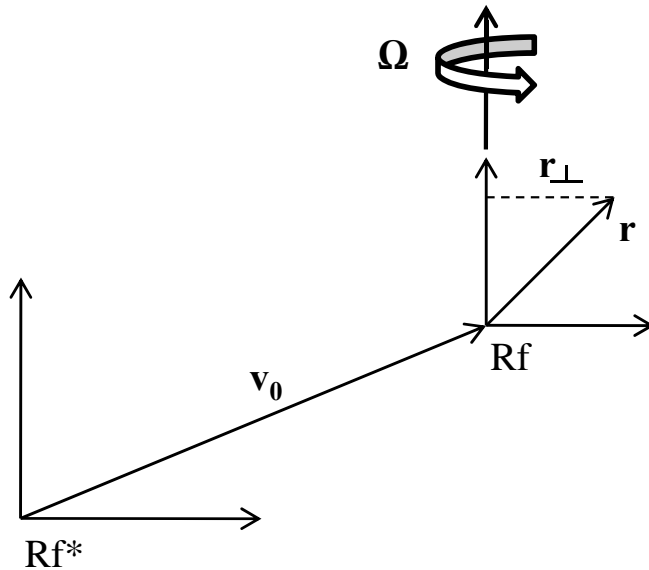
Figure 2.1: A position in the moving reference frame Rf is defined by the position vector $\boldsymbol{r}$. Rf moves relative to the stationary reference frame Rf* with a translational velocity $\boldsymbol{v_0}$ and an angular velocity $\boldsymbol{\Omega}$.

2.2   System rotation

Most engineering problems are analysed in a stationary coordinate system. We may name this absolute (inertial) reference frame Rf*. Some problems are however easier to work with in a moving coordinate system which is fixed to a relevant physical object in the problem. The moving reference frame Rf may, for instance, be rotating with the same angular velocity as a shaft or a duct in a given problem. Primary sources for the current section are Andersson [2] and Kundu & Cohen [29, sec. 4.12].

A general dynamical problem is to be considered in the moving reference frame Rf, as seen in figure 2.1. Rf moves with a velocity $\boldsymbol{v_0}$ and accelerates with $\boldsymbol{a_0}$ relative to Rf*. Rf is also rotating with the an angular velocity, where the rotation rate and direction are given by $\boldsymbol{\Omega}$.

The absolute velocity $\boldsymbol{v^*}$ in Rf* can be related to the relative velocity $\boldsymbol{v}$ at

a given place r in Rf by

$$v^* = v_0 + \Omega \times r + v. \tag{2.3}$$

Similarly, the acceleration a^* in Rf* can be expressed as

$$a^* = a_0 + \dot{\Omega} \times r + \Omega \times (\Omega \times r) + 2\Omega \times v + a, \tag{2.4}$$

where $\dot{\Omega}$ is the angular velocity vector differentiated with respect to time and a is the acceleration seen in Rf. $2\Omega \times v$ is the Coriolis acceleration.

The linear momentum within a volume $\mathcal{V}$ is $q = \int_\mathcal{V} v\rho d\mathcal{V}$. Euler's first axiom states that $f = \dot{q} \Rightarrow f = \int_\mathcal{V} \dot{v}\rho d\mathcal{V} = \int_\mathcal{V} a\rho d\mathcal{V}$, where f is the forces acting on the mass $\rho d\mathcal{V}$. If we apply this to the moving reference frame and utilise equation (2.4), we get an expression for the forces acting in Rf:

$$f = \int_\mathcal{V} a^* \rho d\mathcal{V} + \int_\mathcal{V} -(a_0 + \dot{\Omega} \times r + \Omega \times (\Omega \times r))\rho d\mathcal{V} + \int_\mathcal{V} -2\Omega \times v\rho d\mathcal{V} \tag{2.5}$$

Equation (2.5) shows that fictitious forces must be introduced in order to make the equations of translational motion valid in a moving coordinate system. These forces are fictitious in the sense that they do not obey Newton's third law, there are no counter forces. $\int_\mathcal{V} -2\Omega \times v\rho d\mathcal{V}$ is the Coriolis force and $-\int_\mathcal{V} \Omega \times (\Omega \times r)\rho d\mathcal{V}$ is the centrifugal force.

$\Omega \times (\Omega \times r)$ may be written in terms of the vector $r_\perp$, perpendicular to the rotation axis. As seen in figure 2.1, $\Omega \times r = \Omega \times r_\perp$ and $\Omega \cdot r_\perp = 0$. Using this together with the vector identity $A \times (B \times C) = (A \cdot C)B - (A \cdot B)C$, we obtain a simpler expression for the centripetal acceleration:

$$\Omega \times (\Omega \times r) = -(\Omega \cdot \Omega)r_\perp = -\Omega^2 r_\perp \tag{2.6}$$

The equation of motion for incompressible fluid flow (eq. (2.2)) can now be transformed to account for rotation in a frame of reference Rf. We simplify and assume constant rotation speed, $\dot{\Omega} = 0$, in addition to no acceleration of Rf relative to Rf*, $a_0 = 0$. By using (2.5) together with (2.6), we get:

$$\frac{\partial U}{\partial t} + (U \cdot \nabla)U = -\frac{1}{\rho}\nabla P + \nu\nabla^2 U + \Omega^2 r_\perp - 2\Omega \times U \tag{2.7}$$

The centrifugal force may be modified, $\Omega^2 r_\perp = \nabla(\frac{1}{2}\Omega^2 r_\perp^2)$, making it possible to combine this term with the pressure force to define the *effective*

7
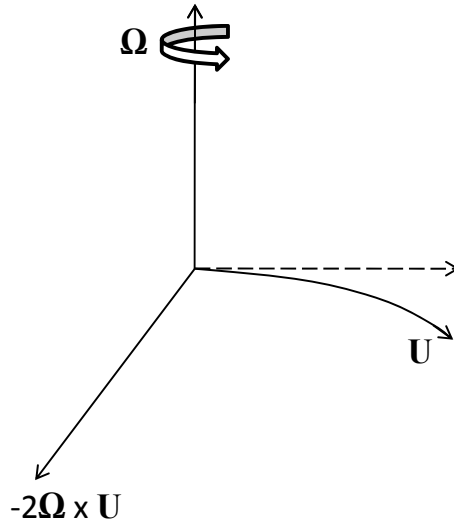
Figure 2.2: The Coriolis force deflects a bullet to the right (westwards) if shot horizontally from the North pole. The stapled line represents the initial velocity.

pressure $P_{\text{eff}} = P - \frac{1}{2}\rho\Omega^2 \boldsymbol{r}_\perp^2$. The centrifugal force is hereby not dynamically significant. The Navier–Stokes equation in a rotating reference frame becomes:

$$\frac{\partial \boldsymbol{U}}{\partial t} + (\boldsymbol{U} \cdot \nabla)\boldsymbol{U} = -\frac{1}{\rho}\nabla P_{\text{eff}} + \nu\nabla^2\boldsymbol{U} - 2\boldsymbol{\Omega} \times \boldsymbol{U} \qquad (2.8)$$

2.2.1 The Coriolis force

The effect of the Coriolis force can be illustrated by looking at the rotating Earth from a stationary reference frame Rf*. In the northern hemisphere, the angular velocity vector $\boldsymbol{\Omega}$ points out of the ground. A particle with a given velocity $\boldsymbol{U}$ will then be deflected to the right of its direction by the Coriolis force $-2\boldsymbol{\Omega} \times \boldsymbol{U}$. Similarly, the deflection is to the left in the southern hemisphere, as $\boldsymbol{\Omega}$ points into the ground. A specific example is a bullet which is shot horizontally from the north pole with a speed U, see figure 2.2.

8

The speed of the bullet will remain constant (neglecting drag), as the Coriolis force $2\Omega U$ acts perpendicular to $\boldsymbol{U}$ at all times. When the bullet has travelled a forward distance of Ut in time t, it has been deflected ΩUt^2. The angular deflection becomes $\Omega Ut^2/Ut = \Omega t$, which corresponds to Earth's rotation in time t. Hence, the bullet does actually travel in a straight line, seen from the inertial outer space (Rf*). The deflection seen on Earth is due to the increasing peripheral speed of the Earth as the bullet moves south. In the rotating reference frame, we need an imaginary force to account for this apparent deflection. However, in general industrial engineering problems, we do not need to account for the Coriolis force due to Earth's rotation. This is because the length scales of such a problem are normally very small compared to the length scales of Earth. Thus, the Coriolis force becomes negligible. Further physical explanation of the Coriolis force, including relevant applications to mechanics, is given by Stommel & Moore [72].

2.2.2   Flow characterisation

A rotating flow is characterised by two dimensionless quantities, the Reynolds number Re and the rotation number Ro. By introducing a velocity scale $\mathcal{U}$, and a length scale $\mathcal{L}$, we define the Reynolds number as

$$Re = \frac{\rho \mathcal{L} \mathcal{U}}{\mu}. \qquad (2.9)$$

The Reynolds number is the ratio of inertial forces to viscous forces, such that viscous effects become increasingly important as Re is reduced.

The Coriolis force affects flows in rotating reference frames to a certain extent, depending on the amount of system rotation. This can be quantified with the rotation number Ro, where the angular velocity is normalised with a time scale:

$$Ro = \frac{\Omega \mathcal{L}}{\mathcal{U}} \qquad (2.10)$$

Additionally, the influence of the Coriolis force due to imposed system rotation depends both on the magnitude and the orientation of the system vorticity $2\boldsymbol{\Omega}$, relative to the local mean flow vorticity $\boldsymbol{\omega} \equiv \nabla \times \boldsymbol{U}$ in a rotating reference frame. In simple shear flows (e.g. plane Poiseuille flow),

9

$\boldsymbol{\omega}$ is perpendicular to both the mean flow direction and the wall-normal direction. If $\boldsymbol{\Omega}$ is in the same or opposite direction as $\boldsymbol{\omega}$, we may look at the *local* rotation number S to effectively distinguish between different flow regimes.

$$S = \frac{2\Omega}{\omega} \tag{2.11}$$

The sign of S depends on whether the fluid vorticity is parallel $(S > 0)$ or anti-parallel $(S < 0)$ with the system vorticity. The first case, with $S > 0$, corresponds to *cyclonic* rotation, meaning that the fluid rotates in the same direction as the system. For $S < 0$, we have *anti-cyclonic* rotation, where the fluid rotates in the opposite direction of the system rotation.

2.3   The RANS equations

Equation (2.1) and (2.8) are valid for all laminar and turbulent flows. It is possible to solve these equations by direct numerical simulation (DNS), but when a flow is turbulent, the fluid motion is disordered, time-dependent and three-dimensional. The scales of turbulent motion vary from the geometric constraints of the flow case, down to the small scales determined by viscous action. Hence, a high resolution is required in both space and time for all scales to be resolved in a DNS. This is very computationally demanding, especially for high-Reynolds number flows. A simpler description of turbulent flow is required for solving practical engineering problems.

Using Reynolds decomposition, we write the instantaneous velocity as $\boldsymbol{U} = \boldsymbol{u} + \boldsymbol{u'}$, where $\boldsymbol{u}$ is the mean (time-averaged) component and $\boldsymbol{u'}$ is the fluctuating component. By inserting this into the continuity equation and Navier–Stokes equations and then averaging in time (denoted by overbar), we can utilise the statistics of turbulence ($\overline{\boldsymbol{u'}} = 0$) to get the so-called Reynolds-averaged Navier–Stokes (RANS) equations for the mean flow:

$$\nabla \cdot \boldsymbol{u} = 0 \tag{2.12}$$

$$\frac{\partial \boldsymbol{u}}{\partial t} + (\boldsymbol{u} \cdot \nabla)\boldsymbol{u} = -\frac{1}{\rho}\nabla p_{\text{eff}} + \nu\nabla^2 \boldsymbol{u} - 2\boldsymbol{\Omega} \times \boldsymbol{u} - \nabla \cdot \overline{\boldsymbol{u'}\boldsymbol{u'}} \tag{2.13}$$

p_{eff} is the effective mean pressure. The new supposed stress tensor, $\overline{u_i' u_j'}$, seen in equation (2.13) represent the effect of turbulence on the mean flow. It comes from the non-linear convective derivative in equation (2.8), so its components actually represent the averaged effect of turbulent convection. This may be seen as diffusion of momentum by turbulence, analogous to diffusion by viscosity which appears as viscous stress in the momentum equations. This explains why the tensor is often called the Reynolds stress tensor.

2.4   Eddy-viscosity turbulence models

If we want to solve the RANS equations, we encounter a closure problem. Solving for the mean, or first moment, requires knowledge of the second moment (Reynolds stresses), as seen in (2.13). This is due to the quadratic nonlinearity in the Navier–Stokes equations. As we will see later, the second-moment equation will contain third moments, so further statistical manipulation of the equations will obviously not lead to closure. Hence, semi-empirical modelling is required in order to obtain a solution.

Following the analogy between the Reynolds stresses and viscous stresses, one simple modelling approach is to introduce an eddy viscosity. More specifically, we assume that there is a tensorally linear relation between stress and strain in the mean flow. Viscous stresses and Reynolds stresses are both linked to the rate of deformation of fluid elements (rate of strain) by the eddy viscosity. The most widely used turbulence models today employ this technique, referred to as the Boussinesq hypothesis. Introducing the turbulent kinetic energy

$$k \equiv \frac{1}{2}\overline{u_i' u_i'}, \tag{2.14}$$

the Reynolds stresses are given by

$$\rho \overline{u_i' u_j'} = \frac{2}{3}\rho k \delta_{ij} - \mu_t \left(\frac{\partial u_i}{\partial x_j} + \frac{\partial u_j}{\partial x_i} \right), \tag{2.15}$$

where μ_t is the eddy viscosity and δ_{ij} is the Kronecker delta. The eddy viscosity is then defined in different ways in various turbulence models. The assumptions which the eddy-viscosity hypothesis is founded on can lead to inaccurate predictions and will be discussed later.

2.4.1 The k–ε model

In modern CFD analysis, the k–ε model is the most used and validated turbulence model. It has been developed and improved over the years, but Jones & Launder [25] are often credited as the developers of the standard k–ε model. As a two-equation model, it allows both the turbulent velocity and length scales to be determined independently. The two equations solved are the transport equations for the turbulent quantities k and ε, where ε is the rate of dissipation of turbulent kinetic energy in dimensions $\mathrm{m}^2/\mathrm{s}^3$. We can define a velocity scale $\mathcal{U} = k^{1/2}$ and a length scale $\mathcal{L} = k^{3/2}/\varepsilon$. The eddy viscosity is then specified as

$$\mu_t = \rho C_\mu \mathcal{U} \mathcal{L} = \rho C_\mu \frac{k^2}{\varepsilon}, \tag{2.16}$$

where C_μ is a constant. The transport equation for k is mathematically derived and originates from the second-moment equation, while the transport equation for ε is best viewed as entirely empirical. They can be written as [3, sec. 4.3.1]

$$\frac{\partial}{\partial t}(\rho k) + \frac{\partial}{\partial x_i}(\rho k u_i) = \frac{\partial}{\partial x_j}\left[\left(\mu + \frac{\mu_t}{\sigma_k}\right)\frac{\partial k}{\partial x_j}\right] + \mathcal{P} - \rho\varepsilon, \tag{2.17}$$

$$\frac{\partial}{\partial t}(\rho\varepsilon) + \frac{\partial}{\partial x_i}(\rho\varepsilon u_i) = \frac{\partial}{\partial x_j}\left[\left(\mu + \frac{\mu_t}{\sigma_\varepsilon}\right)\frac{\partial\varepsilon}{\partial x_j}\right] + C_{1\varepsilon}\frac{\varepsilon}{k}\mathcal{P} - C_{2\varepsilon}\rho\frac{\varepsilon^2}{k}. \tag{2.18}$$

The production of k, $\mathcal{P}$, is defined as

$$\mathcal{P} \equiv -\rho\overline{u_i' u_j'}\frac{\partial u_j}{\partial x_i}, \tag{2.19}$$

and is evaluated as

$$\mathcal{P} = 2\mu_t s_{ij} s_{ij} \tag{2.20}$$

through the Boussinesq hypothesis. The mean strain-rate tensor is given as

$$s_{ij} = \frac{1}{2}\left(\frac{\partial u_i}{\partial x_j} + \frac{\partial u_j}{\partial x_i}\right). \tag{2.21}$$

The dissipation is defined as $\varepsilon = 2\nu\overline{s_{ij}' s_{ij}'}$, where s_{ij}' is the fluctuating rate-of-strain tensor, $s_{ij}' = \frac{1}{2}\left(\frac{\partial u_i'}{\partial x_j} + \frac{\partial u_j'}{\partial x_i}\right)$. Following Launder & Spalding [33],

12

standard values for the model constants are:

$$C_{1\varepsilon} = 1.44, \ \ C_{2\varepsilon} = 1.92, \ \ C_\mu = 0.09, \ \ \sigma_k = 1.0, \ \ \sigma_\varepsilon = 1.3 \qquad (2.22)$$

Equation (2.13) is now closed and can be solved by (2.17), (2.18) and (2.16). Within the eddy viscosity hypothesis lies an assumption of a balance between production and dissipation. This is only reasonable when the mean velocity gradients and turbulence characteristics evolve slowly. In any case, the standard k–ε turbulence model is a simple and well validated model which performs well in several industrially relevant flows.

2.4.2 The Realizable k–ε model

The Realizable k–ε model was developed by Shih *et al.* [59] and yields improved results over the standard k–ε model in flow cases involving rotation, vortices, recirculation and separation [3, sec. 4.3.3]. Comparing with the standard k-ε model, the transport equation for ε is now derived from the vorticity fluctuations. Also, a new definition for the eddy viscosity is introduced based on the realisability constraints; that the normal Reynolds stresses cannot be negative, and the Schwarz' inequality for turbulent shear stress. As in all k–ε turbulence models, the eddy viscosity is computed from equation (2.16), but now C_μ is no longer a constant. It is rather a function of the mean strain and rotation rates, the angular velocity of the system rotation, and k and ε. The transport equations for k and ε can be written as [3, sec. 4.3.3]:

$$\frac{\partial}{\partial t}(\rho k) + \frac{\partial}{\partial x_j}(\rho k u_j) = \frac{\partial}{\partial x_j}\left[\left(\mu + \frac{\mu_t}{\sigma_k}\right)\frac{\partial k}{\partial x_j}\right] + \mathcal{P} - \rho\varepsilon \qquad (2.23)$$

$$\frac{\partial}{\partial t}(\rho\varepsilon) + \frac{\partial}{\partial x_j}(\rho\varepsilon u_j) = \frac{\partial}{\partial x_j}\left[\left(\mu + \frac{\mu_t}{\sigma_\varepsilon}\right)\frac{\partial\varepsilon}{\partial x_j}\right] + \rho\,C_1\sqrt{2s_{ij}s_{ij}}\,\varepsilon - \rho\,C_2\frac{\varepsilon^2}{k + \sqrt{\nu\varepsilon}} \tag{2.24}$$

Where

$$C_1 = \max\left[0.43, \frac{\eta}{\eta+5}\right] \ \text{ and } \ \eta = \sqrt{2s_{ij}s_{ij}}\frac{k}{\varepsilon}. \qquad (2.25)$$

The standard model constants are:

$$C_2 = 1.9, \ \ \sigma_k = 1.0, \ \ \sigma_\varepsilon = 1.2 \qquad (2.26)$$

C_μ is computed from

$$C_\mu = \frac{1}{A_0 + A_s \frac{kU^*}{\varepsilon}}, \tag{2.27}$$

where

$$U^* \equiv \sqrt{s_{ij}s_{ij} + \tilde{\Omega}_{ij}\tilde{\Omega}_{ij}}, \quad \tilde{\Omega}_{ij} = \Omega_{ij} - 3\epsilon_{ijk}\Omega_k. \tag{2.28}$$

Ω_{ij} is the mean rate-of-rotation tensor,

$$\Omega_{ij} = \frac{1}{2}\left(\frac{\partial u_j}{\partial x_i} - \frac{\partial u_i}{\partial x_j}\right), \tag{2.29}$$

ϵ_{ijk} is the alternating symbol and Ω_k is the angular velocity of Rf. A_0 and A_s are constants, given as $A_0 = 4.04$, $A_s = \sqrt{6}\cos\phi$,

$$\phi = \frac{1}{3}\cos^{-1}(\sqrt{6}B), \quad B = \frac{s_{ij}s_{jk}s_{ki}}{\tilde{s}^3}, \quad \tilde{s} = \sqrt{s_{ij}s_{ij}}.$$

2.5 Reynolds stress equation models

The Reynolds stress equation models (RSMs) are probably the most general of all classical turbulence models and have proven to yield very accurate predictions of mean flow properties in several cases. The models are however complex, as all the Reynolds stresses are computed independently. On the other hand, this is exactly what gives RSMs an advantage over simpler turbulence models. In the k–ε models for instance, turbulence is represented with a scalar quantity k. This makes them unable to simulate the anisotropy of the normal Reynolds stresses, $\overline{u'^2} \neq \overline{v'^2} \neq \overline{w'^2}$, which exists in all real flows. Anisotropy effects may not be important in some industrially relevant flows where simple and efficient models have been preferred. But in flow cases featuring complex strain fields or significant body forces, it is necessary to account for the directional effects of the Reynolds stress field. This is done by abandoning the isotropic eddy-viscosity hypothesis, and closing the RANS equations (eq. (2.12) and (2.13)) by solving transport equations for the Reynolds stresses. The downside to it all is that RSM simulations are computationally expensive and lengthy. In two-dimensional simulations, five "extra" transport equations have to be solved, and without the aid of numerically stabilising eddy viscosities, convergence is slow and may be hard to reach at all. The models are also not widely validated and the results are not flawless, due to the unavoidable modelling.

2.5.1 Transport equations

The equation for the second moment may be derived from the equation for the fluctuating velocity. Third moments and other unknowns appear in this process, which means that modeling is required in order to close the equations. Launder *et al.* [31] is credited for deriving the foundation of the RSM, and the transport equations are given in Fluent [3, sec. 4.8.2] as:

$$
\underbrace{\frac{\partial}{\partial t}\left(\rho\overline{u_i' u_j'}\right)}_{\text{Time derivative}} + \underbrace{\frac{\partial}{\partial x_k}\left(\rho u_k \overline{u_i' u_j'}\right)}_{C_{ij} \equiv \text{Convection}} = \underbrace{-\frac{\partial}{\partial x_k}\left[\rho\overline{u_i' u_j' u_k'} + \overline{p'\left(\delta_{kj}u_i' + \delta_{ik}u_j'\right)}\right]}_{D_{T,ij} \equiv \text{Turbulent diffusion}}
$$

$$
+ \underbrace{\frac{\partial}{\partial x_k}\left[\mu\frac{\partial}{\partial x_k}\left(\overline{u_i' u_j'}\right)\right]}_{D_{L,ij} \equiv \text{Molecular diffusion}} \underbrace{-\rho\left(\overline{u_i' u_k'}\frac{\partial u_j}{\partial x_k} + \overline{u_j' u_k'}\frac{\partial u_i}{\partial x_k}\right)}_{P_{ij} \equiv \text{Stress production}} + \underbrace{\overline{p'\left(\frac{\partial u_i'}{\partial x_j} + \frac{\partial u_j'}{\partial x_i}\right)}}_{\phi_{ij} \equiv \text{Pressure strain}}
$$

$$
- \underbrace{2\mu\overline{\frac{\partial u_i'}{\partial x_k}\frac{\partial u_j'}{\partial x_k}}}_{\varepsilon_{ij} \equiv \text{Dissipation}} \underbrace{-2\rho\Omega_k\left(\overline{u_j' u_m'}\epsilon_{ikm} + \overline{u_i' u_m'}\epsilon_{jkm}\right)}_{F_{ij} \equiv \text{Production by system rotation}} \tag{2.30}
$$

Models for diffusion $D_{T,ij}$, redistribution ϕ_{ij} and dissipation ε_{ij} are required in order to close (2.30).

2.5.2 Modelling diffusion

The diffusion term $D_{T,ij}$ can be modelled by assuming that the rate of transport of Reynolds stresses by diffusion is proportional to gradients of Reynolds stresses. See the hypothesis by Daly & Harlow [10]. Due to numerical instabilities, the model is often simplified to a isotropic model by introducing the eddy viscosity μ_t [74, chapter 3.7.3]. Fluent uses the scalar turbulent diffusivity given in Lien & Leschziner [37]:

$$
D_{T,ij} = \frac{\partial}{\partial x_k}\left(\frac{\mu_t}{\sigma_k}\frac{\partial\overline{u_i' u_j'}}{\partial x_k}\right) \tag{2.31}
$$

Here, the Prandtl number for turbulence energy is $\sigma_k = 0.82$, derived on basis of planar homogeneous shear flow. As in the standard k–ε model, μ_t is given by equation (2.16) with $C_\mu = 0.09$.

2.5.3 Modelling dissipation

Dissipation of the Reynolds stresses, ε_{ij}, is modelled by assuming isotropy of the small dissipative eddies. In practice, this can be done by relating ε_{ij} to the isotropic ε, the dissipation rate of turbulent kinetic energy.

$$\varepsilon_{ij} = \frac{2}{3}\rho\varepsilon\delta_{ij} \tag{2.32}$$

This is accurate for high-Reynolds-number flows, but some anisotropy do occur when the flow has a moderate Reynolds number [66]. We may however account for this by absorbing the anisotropic component $\varepsilon_{ij} - \frac{2}{3}\varepsilon\delta_{ij}$ into the model for the pressure-strain term ϕ_{ij}. In the region near walls the dissipation is anisotropic, calling for other models, which will be discussed later.

The transport equation for ε is

$$\frac{\partial}{\partial t}(\rho\varepsilon) + \frac{\partial}{\partial x_i}(\rho\varepsilon u_i) = \frac{\partial}{\partial x_j}\left[\left(\mu + \frac{\mu_t}{\sigma_\varepsilon}\right)\frac{\partial\varepsilon}{\partial x_j}\right] + \frac{1}{2}C_{\varepsilon 1}\frac{\varepsilon}{k}P_{ii} - C_{\varepsilon 2}\rho\frac{\varepsilon^2}{k}, \tag{2.33}$$

where $\sigma_\varepsilon = 1.0$, $C_{\varepsilon 1} = 1.44$ and $C_{\varepsilon 2} = 1.92$.

2.5.4 Modelling redistribution

The pressure-strain term ϕ_{ij} is difficult to model accurately. The effects on Reynolds stresses by pressure-strain interactions is that energy is redistributed between the normal Reynolds stresses ($i = j$), making them more isotropic, and that Reynolds shear stresses ($i \neq j$) are reduced. In the modelling process, the flow is taken to be homogeneous and the redistribution is usually decomposed into a slow part and a rapid part:

$$\phi_{ij}^h = \phi_{ij}^{\text{slow}} + \phi_{ij}^{\text{rapid}} \tag{2.34}$$

The slow part of the model is also known as the return-to-isotropy term, and covers the terms that are not dependent on $\frac{\partial u_i}{\partial x_j}$. When the mean shear is not involved, there is no turbulence production and anisotropy is gradually reduced. The rapid part of the model contains terms involving

16

velocity gradients, which causes them to change instantaneously when the mean flow is altered.

The *Linear Pressure-Strain Model* in Fluent has its foundation in the Gibson–Launder model [17] (see also [30]) and employ a linear model [58] for ϕ_{ij}. The terms in equation (2.34) are given as [3, sec. 4.8.4]:

$$\phi_{ij}^{\text{slow}} \equiv -C_1 \rho \, \frac{\varepsilon}{k} \left[\overline{u_i' u_j'} - \frac{2}{3} \delta_{ij} k \right] \tag{2.35}$$

$$\phi_{ij}^{\text{rapid}} \equiv -C_2 \left[(P_{ij} + F_{ij} - C_{ij}) - \frac{1}{3} \delta_{ij} (P_{kk} - C_{kk}) \right] \tag{2.36}$$

P_{ij}, F_{ij} and C_{ij} are defined as in equation (2.30). C_1 and C_2 will be given in the next section, by (2.39) and (2.40), respectively.

Non-homogeneous effects

Equations (2.35) and (2.36) are derived on basis of the assumption of homogeneous turbulence. Even though no real flow is homogeneous, they are still applicable to regions where variables are functions of position. The variables cannot however, vary rapidly in space. (Quasi-homogeneous conditions.) In some regions this condition is violated, such as in the vicinity of walls. The effect of such non-homogeneities must be added explicitly to the model. [15, sec. 7.3]

Close to a wall, there is a region of strong shear and large rates of turbulent production. The shear and the solid wall itself causes the wall-normal component of turbulence to be suppressed relative to the other components. There are nonlocal effects where pressure fluctuations are enhanced because of the reflected pressure waves (pressure echo), and the wall boundary conditions cause kinematic blocking (see [22]). Such nonlocal kinematics affect the properties of the flow. This is a region where viscous effects are dominant, and the flow is inhomogeneous up to a certain distance relatively far from the wall.

As the suppression of the wall-normal component of turbulence is not captured in the homogeneous part of the model, a correction term is clearly

needed. A wall-echo contribution, or wall-reflection term, is added to the model for redistribution:

$$\phi_{ij} = \phi_{ij}^h + \phi_{ij}^{\text{wall}} = \phi_{ij}^{\text{slow}} + \phi_{ij}^{\text{rapid}} + \phi_{ij}^{\text{wall}} \qquad (2.37)$$

ϕ_{ij}^{wall} is a function of the unit wall normal and the distance to the nearest wall.

$$\begin{aligned}
\phi_{ij}^{\text{wall}} \equiv & C_1' \frac{\varepsilon}{k} \left(\overline{u_k' u_m'} n_k n_m \delta_{ij} - \frac{3}{2} \overline{u_i' u_k'} n_j n_k - \frac{3}{2} \overline{u_j' u_k'} n_i n_k \right) \frac{C_\mu^{\frac{3}{4}} k^{\frac{3}{2}}}{\kappa \varepsilon d} \\
& + C_2' \left(\phi_{km}^{\text{rapid}} n_k n_m \delta_{ij} - \frac{3}{2} \phi_{ik}^{\text{rapid}} n_j n_k - \frac{3}{2} \phi_{jk}^{\text{rapid}} n_i n_k \right) \frac{C_\mu^{\frac{3}{4}} k^{\frac{3}{2}}}{\kappa \varepsilon d}
\end{aligned} \qquad (2.38)$$

Here, n_k is the x_k component of the unit normal to the wall. d is the normal distance to the wall, κ is the von Kármán constant $\kappa = 0.4187$ and $C_\mu = 0.09$. The empirical C_1, C_2, C_1' and C_2' are functions of the Reynolds stress invariants and the turbulent Reynolds number Re_t. They have been selected on basis of comparison with experiments, and are defined as suggested by Launder & Shima [32]:

$$C_1 = 1 + 2.58 A A_2^{1/4} \left\{ 1 - \exp \left[-(0.0067 Re_t)^2 \right] \right\} \qquad (2.39)$$

$$C_2 = 0.75\sqrt{A} \qquad (2.40)$$

$$C_1' = -\frac{2}{3} C_1 + 1.67 \qquad (2.41)$$

$$C_2' = \max \left[\frac{\frac{2}{3} C_2 - \frac{1}{6}}{C_2}, 0 \right] \qquad (2.42)$$

$$Re_t = \frac{\rho k^2}{\mu \varepsilon} \qquad (2.43)$$

$$A \equiv \left[1 - \frac{9}{8} (A_2 - A_3) \right], \quad A_2 \equiv b_{ik} b_{ki}, \quad A_3 \equiv b_{ik} b_{kj} b_{ji} \qquad (2.44)$$

b_{ij} is the Reynolds-stress anisotropy tensor,

$$b_{ij} = \frac{\overline{u_i' u_j'} - \frac{2}{3} \delta_{ij} k}{k}. \qquad (2.45)$$

2.6 Discretisation

A problem needs to be discretised if it is to be solved numerically. To do this, Fluent uses the so-called finite volume method. This involves discretisation in space, and in time if the problem is transient. Spatial discretisation is done by dividing the flow domain into several discrete control volumes, or *cells*. A node is placed in the center of each control volume. This allows us to integrate the governing equations over the control volume to get a discretised equation at its node [74, chapter 4]. If this is done for each node in the flow domain, we get a system of linear equations which can be solved in order to obtain a given property at the nodal points. When discretised equations for all nodal points in the flow domain have been set up, the resulting system of linear equations can be solved by iteration.

If the problem involves convection, the flux at the cell faces needs to be known, and a flux balance for each cell is introduced. Convection influences the flow properties only in the flow direction, and it is therefore expected that the property value depends heavily on the corresponding upstream value, rather than the downstream value. The central differencing scheme is thereby not a good option for interpolation, as it does not identify the flow direction. Several schemes which account for upstream influence have consequently been developed, where the simplest one is *the upwind differencing scheme*. Here, the convected value of the property at the cell face is taken to be equal to the value at the upstream node.

Representing fluid flow equations in a discrete form will inevitably lead to errors. Numerical diffusion arise from truncation errors occurring during interpolation. The upwind differencing scheme is only first-order accurate in terms of truncation errors, and higher-order schemes have therefore been developed in order to reduce the effect of numerical diffusion on the solution. These include the second-order upwind scheme, the QUICK scheme and the third-order MUSCL scheme. The second-order upwind scheme achieve higher-order accuracy at cell faces through Taylor series-expansion. Higher order schemes are more accurate, but also more exposed to numerical divergence than the upwind differencing scheme. The latter is therefore often useful in initial calculations in CFD analysis.

2.7 Boundary conditions

At the flow boundaries it is necessary to define boundary conditions in order to close the equations, as there is no cell adjacent to the cell face. It is crucial to define physically realistic and well-posed boundary conditions, since the solution of the flow domain can be seen as an extrapolation of the data defined on the boundary surfaces. Selecting unrealistic values at the boundaries may also cause the simulation to diverge. There are many types of boundaries in different flow cases, and the treatment of them depends on the specific case which is subject to modelling. Boundary conditions relevant to the calculations performed in the present work will be discussed in the following subsections.

2.7.1 Inlet and outlet

At the inlet, flow variables like velocity and turbulence properties must be specified. The turbulence properties can be given in terms of e.g. k and ε, and turbulence intensity $I = \frac{(2/3k)^{1/2}}{u} = \frac{u'_{\mathrm{rms}}}{u}$. Values can be found from experimental and DNS data, or by empirical relations. For the RSM, the Reynolds stresses must also be defined at the inlet.

An outlet surface should be placed far away from geometrical obstacles to the flow, where the flow have reached a fully developed state. The reason for this is that the gradient of all flow variables, except pressure, are defined to be zero in the flow direction at the outlet. Zero gauge pressure is usually specified at the outlet.

2.7.2 Walls

At solid walls, the no-slip condition $\boldsymbol{U} = 0$ is applied, leading to the formation of a so-called boundary layer where the mean velocity is less than the mean free-stream velocity. Both the mean velocity field and the turbulence quantities in the flow are thus affected. By considering a Reynolds number $Re_{\mathrm{w}} = \frac{uy}{\nu}$ based on the wall-normal distance y from the wall, we see that Re_{w} will decrease with decreasing y, and viscous forces will eventually become significant compared to the inertia forces. We call this

part of the flow the near-wall region, and we may state that the flow within this region is independent of the free stream parameters. The mean flow velocity will only depend on y, ρ, μ and the wall shear stress τ_w. Dimensional analysis now allows us to introduce the non-dimensional groups u^+ and y^+,

$$u^+ = \frac{u}{u_\tau} = f\left(\frac{\rho u_\tau y}{\mu}\right) = f(y^+) \tag{2.46}$$

where the velocity scale $u_\tau = (\tau_\mathrm{w}/\rho)^{1/2}$ is the so-called friction velocity. The near-wall region may now be divided into three sublayers by means of y^+. Next to the wall we have the viscous sublayer where the flow is dominated by viscous effects. This layer is extremely thin, $y^+ < 5$, and may be regarded as nearly laminar. For values of y^+ between 5 and about 50, we find the buffer layer where effects of viscosity and turbulence are equally important. For a distance outside the buffer layer, the flow is fully turbulent, but viscosity effects are still significant. The region may be called the fully turbulent layer, and ranges from $y^+ \approx 50$ to $y^+ \approx 500$, depending on the free stream Reynolds number.

As most turbulence models primarily are valid for turbulent core flows, the modelling within the near-wall region needs special attention. Equation (2.46) is the foundation for the classical semi-empirical wall functions derived for the different divisions of the boundary layer. If the inner region is not resolved with a fine grid, these may be used in the modelling process. This is cost-efficient, but the functions are unfortunately not accurate for low-Reynolds number flows and become invalid in the case of separation.

There is however another approach where the inner region (viscous sublayer and buffer layer) is resolved with a two-layer model [8]. This is a part of the *enhanced wall treatment* in Fluent, involving new equations for the eddy viscosity μ_t and dissipation ε. The new equations are blended with the standard model equations which apply in the fully turbulent region. This two-layer model is used in both the k–ε models and in the RSM. Defining a turbulent Reynolds number

$$Re_y \equiv \frac{\rho y \sqrt{k}}{\mu}, \tag{2.47}$$

based on the distance to the nearest wall y, the fully turbulent region is defined as $Re_y \geq 200$. Closer to the wall, for $Re_y < 200$, the transport

equation for ε is replaced with the algebraic formula

$$\varepsilon = \frac{k^{3/2}}{\ell_\varepsilon},\tag{2.48}$$

where the dissipation length is calculated as

$$\ell_\varepsilon = yC_\ell^* \left(1 - e^{-Re_y/A_\varepsilon}\right).\tag{2.49}$$

The eddy viscosity μ_t is similarly replaced by $\mu_{t,i}$,

$$\mu_{t,i} = \rho C_\mu \ell_\mu \sqrt{k},\tag{2.50}$$

where the length scale ℓ_μ is calculated as

$$\ell_\mu = yC_\ell^* \left(1 - e^{-Re_y/A_\mu}\right).\tag{2.51}$$

The constants in (2.49) and (2.51) are given as:

$$C_\ell^* = \kappa C_\mu^{-3/4}, \;\; A_\varepsilon = 2C_\ell^*, \;\; A_\mu = 70\tag{2.52}$$

In order to avoid instabilities around $Re_y = 200$, we need to blend the two definitions of μ_t. If $\mu_{t,o}$ is the eddy viscosity in the fully turbulent region, defined in the turbulence model, μ_t is blended as follows:

$$\mu_t = \lambda_\varepsilon \mu_{t,o} + (1 - \lambda_\varepsilon)\mu_{t,i}\tag{2.53}$$

The blending function $\lambda_\varepsilon = \lambda_\varepsilon(Re_y)$ is designed such that it is unity away from walls and zero in the vicinity of walls.

When resolving the inner region with the two-layer model, one should use a structured grid since the flow in a boundary layer mainly moves parallel to the wall. It is also recommended that the value of y^+ at the wall-adjacent cell is close to 1 [3, sec. 4.13.4].

2.8 Large-eddy simulation

As mentioned earlier, equation (2.1) and (2.8) can be solved explicitly by resolving all turbulent scales in a three-dimensional and time-dependent

DNS. But since the computational cost of such a simulation increases as the cube of the Reynolds number, they are only feasible for simple low-Reynolds-number flows. Turbulence modelling (mainly RANS models) on coarser grids has been the solution in many cases. Anyhow, nearly all of the computational effort in a DNS is expended on the small dissipation-range eddies, even though the bulk of energy and anisotropy are contained in the larger scales of motion. Thus, a compromise can be made, where only the large eddies are computed explicitly, while the small eddies are omitted and their influence is represented by a model. In other words, a DNS is performed on a coarse grid and a model accounts for the small eddies that are not resolved. This is the concept of the large-eddy simulation (LES) approach, where Smagorinsky [63], Lilly [38] and Deardorff [11] did much of the pioneering work. LES should apparently be accurate for a wide range of flow problems, since the large-scale motions are geometry dependent, while the influence of the smaller scales is less flow dependent.

The so-called filtering process cuts off small scales and retains the large scale motions by means of a filter function $G(\boldsymbol{x}, \boldsymbol{x'}, \Delta)$. Filtered variables are denoted by a hat, and the filtered (resolved) velocity $\hat{\boldsymbol{U}}$ is

$$\hat{\boldsymbol{U}}(\boldsymbol{x}, t) = \iiint\limits_{-\infty}^{\infty} G(\boldsymbol{x}, \boldsymbol{x'}, \Delta)\boldsymbol{U}(\boldsymbol{x'}, t)dx'dy'dz', \qquad (2.54)$$

where Δ is the cutoff scale which indicates the scale of the smallest retained eddies. Filtering is thus an integration in space and the filter function G may be defined in several ways. The most common filter functions for LES computations are the box filter, the Gaussian filter and the spectral cutoff method. The box filter is used in finite volume implementations of LES, while the other two are more common in research computations. The cutoff scale, or filter width, can be chosen freely, but in finite volume computations it is pointless to choose a value smaller than the grid size. Often the cutoff scale is determined as the cube root of the grid cell volume. [74, sec. 3.8]

The filtered continuity and Navier–Stokes equations can be written as

$$\frac{\partial \hat{U}_i}{\partial x_i} = 0, \qquad (2.55)$$

$$\frac{\partial \hat{U}_i}{\partial t} + \frac{\partial \hat{U}_j \hat{U}_i}{\partial x_j} = -\frac{1}{\rho}\frac{\partial \hat{P}_{\text{eff}}}{\partial x_i} + \nu\frac{\partial^2 \hat{U}_i}{\partial x_j \partial x_j} - 2\epsilon_{ijk}\Omega_j \hat{U}_k - \frac{\partial \tau_{ij}^{\text{SGS}}}{\partial x_j}. \qquad (2.56)$$

The new term

$$\tau_{ij}^{\text{SGS}} = \widehat{U_i U_j} - \hat{U}_i \hat{U}_j \tag{2.57}$$

is called the subgrid stress (SGS) tensor and needs to be modelled in order to close the equations. The modelling task in LES is less demanding than the corresponding modelling in RANS. In LES, the main purpose of the subgrid model is to account for dissipation by the small eddies that were cut off, while the filtered Navier–Stokes equations are responsible for capturing the development of the flow. There is even one implicit LES approach where no subgrid model is used at all [18]. The most popular SGS model however, is the relatively simple Smagorinsky model [63], which is an eddy-viscosity model similar to equation (2.15). The subgrid stresses are given as

$$\tau_{ij}^{\text{SGS}} = -\frac{2}{\rho}\mu_{\text{SGS}}\hat{S}_{ij}, \tag{2.58}$$

where μ_{SGS} is the SGS eddy viscosity and the resolved strain-rate tensor is

$$\hat{S}_{ij} = \frac{1}{2}\left(\frac{\partial \hat{U}_i}{\partial x_j} + \frac{\partial \hat{U}_j}{\partial x_i}\right). \tag{2.59}$$

The eddy viscosity μ_{SGS} is further expressed by means of a velocity scale $\mathcal{U}$ and a length scale $\mathcal{L}$,

$$\mu_{\text{SGS}} = \rho\mathcal{U}\mathcal{L} = \rho\mathcal{L}^2\sqrt{2|\hat{S}|^2}, \tag{2.60}$$

where $|\hat{S}|^2 = \hat{S}_{ij}\hat{S}_{ij}$. An obvious choice of a length scale is a scale proportional to the cutoff scale. We obtain

$$\mu_{\text{SGS}} = \rho(c_s\Delta)^2\sqrt{2|\hat{S}|^2}, \tag{2.61}$$

where the Smagorinsky constant c_s is an empirical constant. Closure is thus achieved, but later studies have revealed that the Smagorinsky constant is flow dependent. Ranging from 0.1 for plane channel flow to 0.2 for isotropic turbulence [15, sec. 13.1.2.1], a dynamic c_s seems more appropriate. Several SGS models have been proposed over the years, and some of them will be discussed in the subsequent chapter.

Chapter 3

Modelling Coriolis-force effects

3.1 Introduction

When we consider flows in rotating coordinate systems, the momentum equations are transformed by adding the Coriolis acceleration. In order to understand how the flow is affected by this, we may consider the transport equations for the individual Reynolds stress components (2.30). The mean shear production P_{ij} and rotational production F_{ij} of Reynolds stresses are given as:

$$\frac{P_{ij}}{\rho} = -\overline{u_i' u_k'} \frac{\partial u_j}{\partial x_k} - \overline{u_j' u_k'} \frac{\partial u_i}{\partial x_k} \tag{3.1}$$

$$\frac{F_{ij}}{\rho} = -2\Omega_k \left(\overline{u_j' u_m'} \epsilon_{ikm} + \overline{u_i' u_m'} \epsilon_{jkm} \right) \tag{3.2}$$

For parallel shear flows (e.g. channel flow) in the xy plane, where the axis of rotation $\boldsymbol{\Omega}$ is in the z direction, the components of (3.1) and (3.2) can be written out as in table 3.1.

The Reynolds shear stress $\overline{u'v'}$ and the mean shear $\partial u/\partial y$ are usually of opposite signs. Independent of any system rotation, interactions between them will cause production of streamwise velocity fluctuations. The production terms for the other normal Reynolds stresses due to mean shear are zero, but some of the energy associated with streamwise velocity fluctuations is redistributed to $\overline{v'^2}$ and $\overline{w'^2}$ through pressure-strain

ij	11	22	33	12
P_{ij}/ρ	$-2\overline{u'v'}du/dy$	0	0	$-\overline{v'^2}du/dy$
F_{ij}/ρ	$4\Omega\overline{u'v'}$	$-4\Omega\overline{u'v'}$	0	$-2\Omega(\overline{u'^2}-\overline{v'^2})$

Table 3.1: Components of Reynolds stress production terms due to mean shear (P_{ij}) and rotation (F_{ij}) in parallel shear flow rotating about the spanwise axis z.

interactions in ϕ_{ij}. The redistribution tends to make the turbulence more isotropic since, usually, $\phi_{11} < 0$ while ϕ_{22} and ϕ_{33} are positive.

When system rotation is imposed, the production term F_{ij} becomes active. Its components are correlations between the fluctuating component of the Coriolis force and a fluctuating velocity component. From table 3.1, it can be seen that the normal Reynolds stresses $\overline{u'^2}$ and $\overline{v'^2}$ are oppositely affected by the system rotation, as the respective production terms always are of opposite sign. Then, by considering the contribution to the turbulent kinetic energy $k = \frac{1}{2}\overline{u_i'u_i'}$,

$$\frac{1}{\rho}\left(\frac{1}{2}P_{ii} + \frac{1}{2}F_{ii}\right) = \frac{1}{2}\left(-2\overline{u'v'}\frac{du}{dy}\right) + \frac{1}{2}(0) = -\overline{u'v'}\frac{du}{dy}, \qquad (3.3)$$

it is seen that k does not directly depend on the system rotation. This can be explained by recalling that the Coriolis force acts perpendicular to the instantaneous velocity vector $\boldsymbol{U}$, and thereby cannot perform any work on the fluid. Hence, the result is valid for all flows, not just parallel shear flow. The Coriolis force may however affect the turbulence energy level indirectly by altering the anisotropy through the production terms in table 3.1.

Consider a region of a parallel shear flow subject to positive rotation $\Omega_z > 0$, where $du/dy > 0$, and the corresponding vorticity becomes negative, $\omega_z = -du/dy$. This signifies anti-cyclonic rotation where S (eq. (2.11)) is negative. P_{12} contributes to the negative shear stress $\overline{u'v'}$, which consequently increases production of $\overline{u'^2}$ through P_{11}. If $\overline{u'^2} > \overline{v'^2}$, the shear stress production due to rotation, F_{12}, will further decrease $\overline{u'v'}$ proportionally with the angular velocity. This causes dampening of the streamwise fluctuations $\overline{u'^2}$ and amplification of the wall-normal fluctuations $\overline{v'^2}$ by F_{11} and F_{22}, respectively. Hence, the turbulence agitation is enhanced

26

(destabilised). However, at high rotation rates, the turbulence agitation restabilises when $\overline{u'^2}$ becomes smaller than $\overline{v'^2}$, causing F_{12} to change sign. In the case of cyclonic rotation, $S > 0$, we have an opposite scenario where the turbulence is dampened. These alterations of the turbulence will naturally affect the mean velocity profile as the flow varies between being highly turbulent and more laminar-like. See e.g. Andersson [1] and Kristoffersen & Andersson [27] for further details. What we can conclude from the preceding illustration, is that even in the simple case of a parallel shear flow, the mean velocity profile is changed when the Reynolds stresses are altered by rotational effects. Being able to account for these effects is therefore a vital part of computations involving rotating flows.

Parallel shear flows are relatively simple and have often been subject of investigation when it comes to rotating flows. Turbulence models are also frequently validated by comparing their results with DNS or experimental data from this kind of flows. The current section illustrates the importance of accounting for Coriolis-force effects when modelling rotating turbulent flows. Different classes of turbulence models respond to system rotation in different ways, depending on their complexity. There is a vast number of turbulence models in the literature, but they can be divided into groups based on their underlying theory. A brief review of developments in turbulence modelling concerning Coriolis-force effects will be given in the following sections. Only modelling relevant to modern CFD analysis will be considered.

3.2   Eddy-viscosity models

Because of their computational low cost and robustness, linear eddy-viscosity models are very popular in industrial CFD analysis. The definition of the Reynolds stresses given in equation (2.15) yields simple and stable turbulence modelling where determination of the eddy viscosity is the only required task in order to close the governing equations.

3.2.1 Linear eddy-viscosity models

On basis of empiricism and dimensional analysis, Spalart & Allmaras [67] derived a transport equation for the eddy viscosity itself. The Spalart–Allmaras (SA) one-equation model is intended for aerodynamic flows, and it has predicted them with good results [5]. The transport equation is valid in the vicinity of walls, and as a one-equation model, it is the simplest complete turbulence model and hereby computationally cost-efficient.

The most popular turbulence models are however two-equation models where the eddy viscosity is determined by means of a velocity scale and a length scale, as in equation (2.16). The scales can be constructed by means of two turbulent quantities, for which two transport equations are solved. The most popular choice is k and ε, as in the standard k–ε model, section 2.4.1. The turbulent kinetic energy k is present in most two-equation models, but several quantities have been proposed as the second variable. For example, the k–ω model is a popular model where the specific dissipation rate $\omega \equiv \varepsilon/k$ is taken as the second variable. The most recent version of the model is described in detail by Wilcox [77]. Variables can also be blended, such as in the SST k–ω model by Menter [41], [44]. Here, ω is calculated near walls, while the equation for ε is applied in the free stream.

Near-wall integration has been an issue with the k–ε models. Avoiding integration by using classical wall functions based on equilibrium assumptions has been a popular approach, but it has proven to yield poor results in complex flows. Specifically, in the case of wall-bounded rotating flows, Kristoffersen & Andersson [27] reported that the mean velocity profiles do not correspond with the semi-logarithmic law $u^+ = 2.5 \ln y^+ + 5.5$, due to stabilising and destabilising Coriolis-force effects. As more computational resources became available, integration to the wall was a natural area of research. New formulations for the eddy viscosity and new transport equations for ε, involving damping functions [47], were introduced in order to obtain better accuracy. These ad-hoc modifications are however somewhat numerically stiff and has been implemented with a varying degree of success. General models which can be used in both the free stream and in the vicinity of walls are preferred.

In 1991, Durbin [12] proposed such an alternative approach, the method of elliptic relaxation. The velocity scale k was replaced by the scalar $\overline{v'^2}$,

which is a more appropriate velocity scale near solid boundaries. The model is often referred to as the v^2–f model. Kinematic blocking near boundaries is indirectly accounted for by solving an elliptic relaxation equation for f, which is a source in the $\overline{v'^2}$ equation. When the linear eddy-viscosity hypothesis is invoked, three transport equations are solved, namely those for k, ε and $\overline{v'^2}$. The model can be regarded as a "light" Reynolds stress model in the sense that $\overline{v'^2}$ is analogous to the normal stress component near surfaces ($\overline{v'^2} \approx v^2$ for $y^+ \leq 10$, [51]), and its transport equation is approximated from the corresponding Reynolds stress transport equation. The eddy viscosity is defined as

$$\mu_t = \rho c_\mu \overline{v'^2} T, \tag{3.4}$$

where T is a time scale and c_μ is a constant.

The linear eddy-viscosity models discussed in the previous paragraphs are some of the most popular turbulence models in the CFD community. They do however have some deficiencies in common, which are inherited from their formulation. Related to system rotation, the isotropic eddy viscosity and the material frame-indifference stands out as the most critical issues. As a consequence of the Boussinesq approximation (2.15), where a direct proportionality between the Reynolds stresses and the mean rate of strain is assumed, anisotropy in the normal Reynolds stresses cannot be accounted for. Also, there are no rotation-dependent terms in (2.15), the Reynolds stresses exclusively depend on the frame-indifferent strain-rate tensor, making the previously mentioned models insensitive to Coriolis-force effects. They will only be able to exhibit changes in the pressure and velocity field that stems directly from the centrifugal and Coriolis force terms in the RANS equation (2.13).

3.2.2   Nonlinear eddy-viscosity models

The models may however be sensitised to rotation with model extensions. Simple, case-dependent extensions have been proposed, but general formulations that are frame invariant are of course preferred. Such models can be formulated by e.g. introducing nonlinear dependence on the magnitude of rate of strain and rotation in the eddy-viscosity formulation or in the transport equations. These quasi-linear models are still based on linear

29

tensoral dependence to the rate of strain, but the proportionality coefficient is nonlinear. Quasi-linear and fully nonlinear eddy-viscosity models can be based on the algebraic stress approximation which was introduced in order to reduce the computational expense of solving a full Reynolds stress model. Rodi [56] proposed to reduce the partial differential equations in the RSM to a set of algebraic equations so that $\overline{u_i' u_j'}$ may be implicitly determined by means of mean velocity gradients and transport equations for e.g. k and ε. By structural equilibrium assumptions the physics of the full RSM should be retained in the derived algebraic stress model (ASM). Obviously, the final result depends on the unavoidable modelling. This was the basis for constitutive modelling where the stress tensor is a function of rates of strain and rate of rotation. A general explicit relation can be obtained as a linear combination of ten tensors, as derived by Pope [53]. Retaining only quadratic terms, the general stress tensor function can then be written as [15, sec. 7.2.3]

$$
\begin{aligned}
\overline{u_i' u_j'} - \frac{2}{3}\delta_{ij}k = &- c_1 s_{ij} + c_2 \left(s_{ik}s_{kj} - \frac{1}{3}|\boldsymbol{s}|^2 \delta_{ij} \right) \\
&+ c_3 \left(\Omega_{ik}s_{kj} + \Omega_{jk}s_{ki} \right) + c_4 \left(\Omega_{ik}\Omega_{jk} - \frac{1}{3}|\boldsymbol{\Omega}|^2 \delta_{ij} \right),
\end{aligned}
\tag{3.5}
$$

where $|\boldsymbol{s}|^2 = s_{ij}s_{ij}$ and $|\boldsymbol{\Omega}|^2 = \Omega_{ij}\Omega_{ij}$. Speziale [69] showed that algebraic turbulence models are affected by system rotation only through the intrinsic rotation tensor, which can be obtained by adding the term $C\epsilon_{ijk}\Omega_k$ to the rotation tensor Ω_{ij}. C is a constant derived from the turbulence model in which it is used. The introduction of the intrinsic rotation tensor makes algebraic closures frame-independent and this is employed in the subsequent mentioned models.

c_1, c_2, c_3 and c_4 may be determined in an ad-hoc manner, often based on mathematical constraints, or they can be determined directly from an underlying RSM. In linear eddy-viscosity models, c_2, c_3 and c_4 are set to zero and c_1 is constant, as seen in (2.15). In the quasi-linear models however, c_1 involve nonlinear dependence on the magnitude of rate of strain and rotation. Indeed, it can be shown that the response to system rotation can be captured by an eddy-viscosity model with a variable c_1 [15, sec. 8.3.3].

The Realizable k–ε model in section 2.4.2 is an example of a quasi-linear model where the realisability constraints are invoked when developing the

ad-hoc extension. Computations with this model have yielded rotational effects on the mean flow field, but it is not able to predict turbulence stabilisation [14]. No dependence on rotation will thus be seen in a flow case such as the rotating channel flow [27] where the rotational effects act only through the turbulence equations. Pettersson Reif *et al.* [50] sensitised the v^2–f model by means of an algebraic stress model and were able to capture Coriolis-force effects, including turbulence stabilisation, that the original model could not predict. For the one-equation SA model, turbulence enhancement by Coriolis-force effects corresponds to an increase in the eddy viscosity. Spalart & Shur [68] proposed the Spalart–Shur correction term in the SA transport equation and was able to predict rotational effects. The same correction term is also applicable to other models and has quite successfully been implemented in the SST k–ω model by Smirnov & Menter [64].

In order to account for the anisotropy of the the turbulence field more extensively, the remaining coefficients in equation (3.5) may be non-zero to get a fully nonlinear eddy-viscosity model. Secondary fluid motion normal to the streamwise direction of the flow is linked to turbulence anisotropy. The secondary flows referred to as flows of Prandtl's first and second kind appear in duct flows. The former is due to an imbalance between the pressure and Coriolis forces near walls where the Coriolis force goes to zero. It appears in laminar as well as turbulent rotating flows, and will affect the turbulent fluctuations. See e.g. Speziale [71]. The latter arises due to anisotropies in the turbulence field close to walls and appears also in non-rotating ducts. However, the stabilising effect of rotation modifies the turbulence anisotropy, and should therefore affect the formation of this secondary flow. A third flow phenomena appearing in rotating flows are longitudinal vortices or roll cells. These appear in both rotating ducts and channels due to instabilities in connection with the rotation. Also these will affect turbulence fluctuations. See e.g. [27] and [71].

If a given turbulence model is able to simulate the turbulence anisotropy, it should be able to show secondary flows and in general yield a more accurate solution. Pettersson Reif [49] further developed the model given in [50] and derived a nonlinear v^2–f model by a phenomenological method. The model is reported to predict turbulence anisotropy in wall-bounded flows quite accurately. The lack of a transport mechanism for the Reynolds stresses in

the algebraic formulation is however a drawback for the model. Craft *et al.* [9] proposed a cubic model and provide an overview of some quadratic models in their paper. See also Hellsten & Wallin [21] for further details on the explicit ASM approach, including concerns relevant to system rotation, and recent developments in the field.

3.3   Reynolds stress equation models

In Reynolds stress models, transport equations for the individual Reynolds stresses are solved, namely equation (2.30). The exact term for rotational production F_{ij} appears naturally when deriving the transport equations, and makes second moment closure the natural choice for modelling turbulent flows subject to rotation. The absence of modelling requirements for the production terms P_{ij} and F_{ij}, and the presence of a redistribution term ϕ_{ij}, are the most advantageous properties of the RSM. The differences between various RSMs lie in the modelling of redistribution, dissipation and diffusion, where redistribution modelling is the most complex task.

When it comes to Coriolis-force effects, the behaviour of the production terms was illustrated by an example in section 3.1, while the modelling of diffusion $D_{T,ij}$ does not require special attention related to rotation. Some considerations are however required for modelling of redistribution and dissipation. As discussed in section 2.5.4, it is common practice to split the redistribution term ϕ_{ij} into slow and rapid parts, as well as a wall-correction part. The resulting tensors ϕ_{ij}^{slow} and ϕ_{ij}^{rapid} can be expanded analogous to equation (3.5), through the Cayley–Hamilton theorem. The obtained equation for ϕ_{ij}^{slow} is quadratic, but only the linear term is retained in most RSMs, according to the Rotta model [58]. An exception is the quadratic model (SSG model) by Speziale *et al.* [70], which is the most general quasi-linear pressure-strain model. Models for ϕ_{ij}^{slow} are not affected by system rotation. ϕ_{ij}^{rapid}, on the other hand, may we written in terms of production, diffusion and the mean strain-rate tensor [31]. Here it is important to account for rotational production by including $1/2 F_{ij}$, in addition to the shear production P_{ij}, in the model. The coefficient of $1/2$ is included to ensure material frame indifference, see e.g. [35]. Several models for the wall-correction term ϕ_{ij}^{wall} have been proposed, including the low-

Re version given in equation (2.38). (Low-Re models can be integrated to the wall.) The purpose of this term is to account for the blocking effect close to walls by proper stress redistribution and modification of the stress production. Rotational effects come into play e.g. through the inclusion of $\phi_{ij}^{\mathrm{rapid}}$ in the model for the latter process.

An early RSM computation of fully developed turbulent flow in a rotating channel was the one by Launder *et al.* [35], published in 1987. The main effects of rotation were successfully captured by the model. Nilsen & Andersson [45] used an ASM based on the very same model to compute the turbulent flow over a rotating backward-facing step. In an ASM formulation, the production terms from the RSM is retained. This made it possible to correctly predict the correlation between reattachment length and rotation rate, as well as turbulence anisotropy. The accuracy in both computations were however rather poor due to the employment of standard wall functions. Better results were obtained by Kristoffersen *et al.* [28] when computations with the low-Re RSM by Launder & Shima [32] were compared with DNS data for rotating channel flow. Launder & Tselepidakis [34] subsequently proposed a new low-Re model which yielded even better results than those reported by Kristoffersen *et al.* [28].

The modelling of redistribution near walls is apparently crucial in second moment closure. Instead of adding wall-correction terms, Durbin [13] introduced the previously discussed elliptic relaxation approach applied to the redistribution term. The blocking effect is now indirectly accounted for by the solution of an elliptic equation. The method can be applied to a variety of second moment closures. Pettersson & Andersson [48] modelled near-wall effects using elliptic relaxation in conjunction with the nonlinear pressure-strain model by Ristorcelli *et al.* [55]. The flow case was fully developed turbulent Poiseuille and Couette flow subjected to spanwise rotation, and the results were compared with DNS data. The model predicted the features of the mean flow and turbulence field quite well, but some significant discrepancies were seen on the stable side of the rotating Poiseuille flow at low rotation numbers and in Couette flow subjected to destabilising rotation. Oberlack *et al.* [46] used the elliptic relaxation method in conjunction with the SSG model to predict the complicated case of turbulent channel flow with streamwise rotation. The model did capture most of the basic features of the flow, but one stress component was

computed with a wrong sign, which was due to a defect in the SSG model. Second moment closure with the elliptic relaxation method has proven to yield good results in several cases, but suffers from numerical stiffness arising from its boundary conditions [15, sec. 7.4.1], and is therefore not widely used in industrial CFD. Extensive research on making models like this less stiff and computationally cheaper is ongoing. Proposals like modelling of redistribution by means of a wall effect vector by Shima & Kobayashi [60] show promising results for rotating flows and are encouraging.

In the dissipation modelling, many RSMs make use of the transport equation (2.33) which has no rotation-dependent terms. However, since the transport equation for the governing dissipation rate tensor ε_{ij} *does* contain rotation-dependent terms, equation (2.33) should be modified accordingly. Several proposals on how to do this have been published, including the one by Shimomura [61] where an extra source term is added to the ε transport equation. The addition was used in e.g. Pettersson & Andersson [48] and is elsewhere reported to improve predictions of rotating channel flow [24].

Around year 2000, the always increasing available computational resources triggered the interest for unsteady RANS (URANS) modelling of turbulent flows. Unsteady implies time dependent simulations, which is a natural pre-requisite for flows that are not statistically stationary. The computations can be performed in both two and three dimensions. Three-dimensional computations are however required in order to predict important flow features in massively separated flows. The URANS approach have been examined and validated by e.g. Iaccarino *et al.* [23] and Shur *et al.* [62]. Unsteady three-dimensional computations have become relevant for industrial applications during the last decade, and there is a constant demand for better accuracy. This brings us on to eddy-resolving approaches, which is the topic of the next section. For further details on Reynolds stress equation models in general, see e.g. Hanjalić & Jakirlić [20].

3.4   Eddy-resolving simulations

When turbulent eddies are resolved and simulated, the physics and development of the flow are inherently captured from solving the Navier–Stokes equations. Thus, given a sufficient resolution in space and time,

the influence of e.g. the Coriolis force can be precisely predicted by the computations. However, such high resolutions are not feasible in most situations, calling for approaches where only a portion of the eddies are resolved. As explained in section 2.8, modelling is then normally introduced in order to account for what is omitted. Raufeisen *et al.* [54] showed that it is beneficial to include a SGS model, but its influence on the solution will naturally depend on the cutoff scale. LES computations with a small cutoff scale (high resolution) will be less affected by the SGS model than computations with a large cutoff scale.

LES is in general the most accurate CFD approach where modelling is involved, as the filtered Navier–Stokes equations (2.55) and (2.56) are solved explicitly. Only numerical dissipation and limitations of the SGS model cause incorrectness in LES. Recall that the main purpose of the SGS models in LES is to account for the flow of kinetic energy between resolved eddies and the small eddies that are cut off. It is not necessary to involve the system rotation directly in the SGS model in order to exhibit Coriolis-force effects in the flow, as opposed to RANS models. This is why LES can yield very good results for rotating flows, and it stands out as the main advantage of using LES when predicting these flows, compared to RANS.

Even though system rotation is not directly involved in SGS modelling, the choice of a model is important. In turbulent flows, energy is transferred through the energy cascade from the large scales to the small scales, where it is dissipated by viscous effects. In the context of LES, the energy transfer from the resolved scales to the unresolved scales is termed forward scatter. According to Leslie & Quarini [36], some energy is also transferred the other way, from unresolved scales to resolved scales. Referred to as backward scatter, this could be almost a third of the forward scatter. In rotating flows, the stabilising and destabilising effects of the Coriolis force alters the energy flow between the eddies. As seen in e.g. Xun *et al.* [78], both forward and backward scatter is enhanced in destabilised regions and reduced to nearly zero in stabilised regions. Thus, being able to predict this with the SGS model could be important for LES computations of rotating flows.

The Smagorinsky model described in section 2.8 is a purely dissipative model, predicting forward scatter only. A dynamic SGS model, where the local Smagorinsky constant c_s is determined from the resolved scales, was proposed by Germano *et al.* [16] and modified by Lilly [39]. A second test

filter is applied, and c_s is evaluated using a least-squares approach. In principle, negative values for c_s is now possible and could be considered as the backward scatter effect. The resulting negative SGS eddy viscosity will however destabilise the numerical algorithm considerably. These values are therefore avoided in practical computations, and linear dynamic models are thereby also unable to account for backward scatter. Quite recently, Marstorp *et al.* [40] used the ASM approach to formulate an explicit dynamic SGS model that could predict the anisotropy of the subgrid dissipation quite accurately. When the model was applied to rotating channel flow, the results were better than those from the dynamic model in Lilly [39].

Some nonlinear SGS models have been proposed, such as the dynamic nonlinear model by Wang & Bergstrom [76]. Similar to the advancement from linear to nonlinear eddy-viscosity RANS models, quadratic terms are now retained in the constitutive relation for the SGS stress tensor. Three terms are included in the model, being functions of the resolved rate of strain and the resolved rate of rotation. Backward scatter from the SGS eddies to the filtered eddies is now possible and the model has proven to be numerically stable. Xun *et al.* [78] compared Lilly's dynamic SGS model [39] and the nonlinear model [76] with DNS data for rotating turbulent channel flow with heat transfer. They found that the nonlinear model yielded improved results over the dynamic model for second-order statistics, mainly due to the prediction of backward scatter. The results for the mean velocity were similar for the two models. A relatively cost-efficient second-order central difference scheme was used for spatial discretisation. This is a reasonable choice, as it may very well be used in commercial applications of LES. Also, the scheme will not contaminate the simulations with too much numerical dissipation, as is the case with first-order schemes.

The main disadvantage of LES compared to RANS computations is of course the computational cost. Very fine grids and short time steps are required in order to resolve the turbulence. Especially for wall-bounded flows, which is the case in most rotating flows, the cost is high. The eddies in the near vicinity of a wall are small, yet highly energetic. They should therefore be resolved in order to uphold the accuracy of the simulation. Such a high resolution is however not an alternative in many cases, as the computational cost scales as the Reynolds number to the power 2.4 for the inner boundary layer [52]. As in RANS modelling, damping functions, wall

functions and wall models have been proposed with a varying degree of success. Damping functions and wall functions are not useful for rotating flows, due to Coriolis-force effects near walls. Balaras *et al.* [4] achieved comparatively good results with a two-layer model in rotating channel flow, but another approach has become popular during the past few years.

Detached eddy simulation (DES) originated in the late nineteen nineties (see Spalart [65]) and was intended primarily for high-Re number, massively separated flows. It presented an approach where the near-wall region is modelled by RANS, while large-scale eddies in the rest of the flow domain are resolved by LES. The RANS model will also serve as a SGS model in the LES regions. The resolved eddies are allowed to evolve from instabilities in shear layers, due to a limited eddy viscosity. In practice, this is done by defining a new turbulent length scale for the computations. The DES length scale $\mathcal{L}_{\mathrm{DES}}$ is typically given as

$$\mathcal{L}_{\mathrm{DES}} = \min[\mathcal{L}, C_{\mathrm{DES}} \max(\Delta x, \Delta y, \Delta z)], \qquad (3.6)$$

where $\mathcal{L}$ is the original RANS model length scale, C_{DES} is a constant and $\Delta \boldsymbol{x}$ is the grid spacing. Thus, the RANS formulation is employed when $\mathcal{L}$ is active, while the model is otherwise reduced to a SGS model. The first DES formulation was based on the Spalart–Allmaras model which uses the distance to the wall as $\mathcal{L}$. In this case, it is easy to see that the transition from RANS to LES will occur at a certain distance from the wall, depending on the grid resolution. Indeed, for a sufficiently fine grid, the DES will tend towards a LES.

As demonstrated by Strelets [73], the DES formulation can also be implemented with other RANS models. The turbulent length scale in different models may very well be a function of both time and space. Whether RANS or LES is employed at a certain point will thus depend on the instantaneous local conditions. Viswanathan & Tafti [75] used a SST k–ω DES formulation to predict the flow and heat transfer in a rotating channel with ribs. The results were compared with results from LES and URANS (SST k–ω) computations. Even though the SST k–ω formulation in the DES was not sensitised to system rotation, the DES results exhibited Coriolis-force effects similar to the LES results. The reattachment length of the recirculation zone behind the ribs varied as the system rotation rate increased, rotation-induced secondary flows were predicted, and turbulence
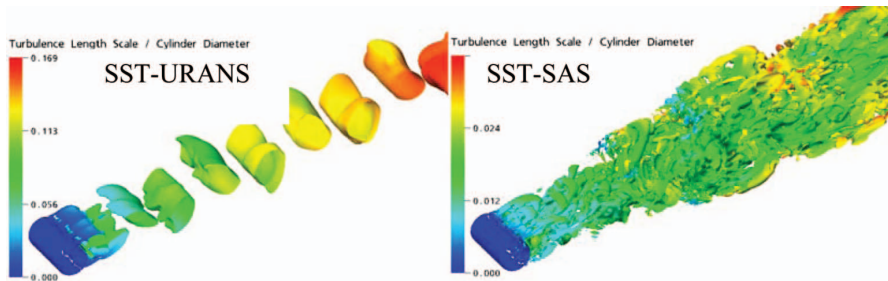
Figure 3.1: Turbulent structures behind a cylinder for a SST URANS and a SST SAS computation. From Menter [42], figure 6.

stabilisation and destabilisation occurred. All at a considerably lower cost than for the LES. The URANS computations showed little or no Coriolis-force effects.

Some DES formulations and other eddy-resolving methods have been implemented in commercial CFD codes during the past few years. The hybrid LES/RANS approach seems to be attractive for industrial CFD applications and will perhaps be the main research area within CFD for the next decade. The motivation is to achieve better accuracy as the computational resources increase. Standard (U)RANS models describe flows in a statistical sense. They will typically produce merely quasi-periodic large-scale unsteady structures, while the chaotic details of turbulence remain unresolved. Resolving more of the turbulence would yield a more detailed and accurate solution for flows that are also governed by the small scale structures. This can be illustrated by comparing the turbulent structures behind a cylinder for the two approaches, as seen in figure 3.1. Here, the eddy-resolving approach is represented by scale adaptive simulation (SAS), see Menter & Egerov [43].

The use of LES and hybrid eddy-resolving methods do however require more knowledge, experience and working hours than RANS computations. It lies in the very nature of eddy resolving that the solution will depend on the grid. The CFD analysist will therefore have to understand turbulent flow physics when constructing a grid that is both cost efficient and fine enough to capture the relevant flow features. Choosing an appropriate time step is
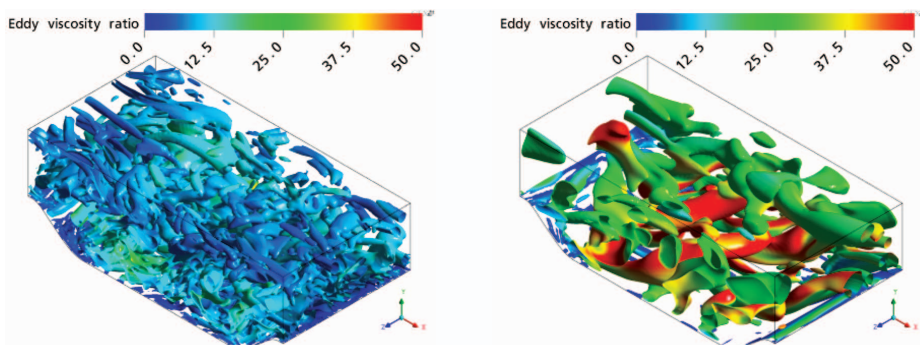
Figure 3.2: Turbulent structures for flow over a periodic hill, using SAS. Left: Short time step. Right: Four times larger time step. From Menter [42], figure 7.

also not trivial. Figure 3.2 illustrates how a SAS solution on the same grid is affected by the time step. The time step in the right part of the figure is increased by a factor of four, compared to the left part. We see that the smallest turbulent structures are not resolved in the simulations with a large time step. Additionally, gathering statistics and post processing of data is a time consuming part of the analysis. Statistical convergence in LES and eddy simulations in general, is slow, and the accumulated data can be overwhelming.

Chapter 4

Flow case and preliminary work

4.1   Flow over a backward-facing step

The flow over a backward-facing step (BFS) in a channel is a geometrically simple flow case which features the physical phenomenas of separation, recirculation and reattachment. The fluid enters upstream of a sudden geometrical expansion and separates from the lower wall at the step edge, as seen in figure 4.1. The separation causes the formation of a anisotropic turbulent free shear layer between the inlet flow and the more stagnant fluid in the step corner. At first, the shear layer is nearly parallel with the walls, but it will soon curve downwards and impinge on the lower wall. We say that the fluid on the low-speed side of the shear layer forms a so-called separation bubble, confined by the walls. An adverse pressure gradient will cause backflow near the lower wall within the separation bubble. The fluid is now recirculating clockwise with a relatively low velocity within the separation bubble, driven by the momentum of the outer flow. There is also a small secondary separation bubble adjacent to the step corner, recirculating in the opposite direction.

For nonrotating high-Re laminar and transitional flows, the flow may detach and reattach at the upper wall, due to the pressure gradient. The fluid
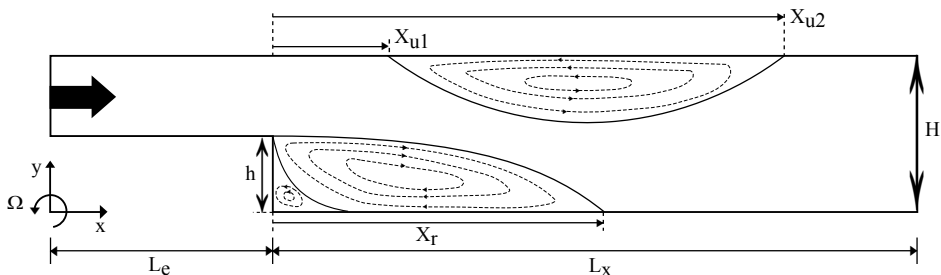
Figure 4.1: Sketch of the spanwise rotating backward-facing step including the recirculation zones.

within the resulting separation bubble will be recirculating in the opposite direction of the fluid within the large recirculation zone near the lower wall. For nonrotating turbulent flows, the separation at the upper straight wall has not been observed. However, when positive (anticlockwise) rotation is induced about the spanwise axis, Barri & Andersson [6] report that this separation bubble occurs also for fully turbulent flows. Notice also that the positive system rotation makes the shear flow along the straight wall cyclonic, $S > 0$, and turbulence is thus dampened. An opposite effect is seen along the stepped wall, where we have anti-cyclonic rotation ($S < 0$) and turbulence augmentation. A mean pressure gradient in the wall-normal direction will also appear in order to balance the y component of the Coriolis force. Consequently, the pressure is in general higher near the stepped wall, than near the straight wall.

At a point where the flow detach or reattach, the wall shear stress

$$\tau_{\mathrm{w}} = \mu \frac{\partial u}{\partial y}\bigg|_{\mathrm{w}} \tag{4.1}$$

is zero. The reattachment length X_r and the corresponding lengths X_{u1} and X_{u2} are thus defined as the distance downstream of the step where τ_{w} is zero. Their value depend on inflow conditions, the system rotation rate, the expansion ratio $ER = h/H$ and the Reynolds number. The latter can be expressed in terms of the inflow bulk velocity $U_b = \frac{1}{\delta} \int_0^\delta u \, dy$ and the step height h,

$$Re_b = U_b h / \nu. \tag{4.2}$$

ij	11	22	33	12
P_{ij}/ρ	$-2\left(\overline{u'^2}\frac{\partial u}{\partial x}+\overline{u'v'}\frac{\partial u}{\partial y}\right)$	$-2\left(\overline{u'v'}\frac{\partial v}{\partial x}+\overline{v'^2}\frac{\partial v}{\partial y}\right)$	0	$-\left(\overline{u'^2}\frac{\partial v}{\partial x}+\overline{v'^2}\frac{\partial u}{\partial y}\right)$
F_{ij}/ρ	$4\Omega\overline{u'v'}$	$-4\Omega\overline{u'v'}$	0	$-2\Omega(\overline{u'^2}-\overline{v'^2})$

Table 4.1: Components of Reynolds stress production terms due to mean shear (P_{ij}) and rotation (F_{ij}) in two-dimensional flow rotating about the spanwise axis z.

δ is half the channel height. The system rotation rate can be be quantified by the dimensionless rotation number Ro given in equation (2.10). In the present study, we define the global rotation number as

$$Ro = \frac{\Omega h}{U_b}. \tag{4.3}$$

Recall the Reynolds stress production terms due to shear and rotation, equations (3.1) and (3.2). The flow over a BFS is two-dimensional, e.g. $\boldsymbol{u} = (u, v, 0)$, and there are consequently more nonzero production terms than in parallel shear flows. The terms are written out in table 4.1. Rotational production is the same as for parallel shear flow, but new terms appear in shear production. The terms involving v can be considered as additional production associated to streamline curvature which will occur downstream of the expansion. The curved shear layer is therefore expected to be highly turbulent.

Barri & Andersson [6] performed a DNS for fully developed turbulent channel flow over a BFS subjected to spanwise rotation. In their case, the expansion ratio was $ER = 1/2$ and the Reynolds number was $Re_b = 5600$. Different rates of positive system rotation was imposed, and the results are consistent with the experimental data provided by Rothe & Johnston [57]. The computational domain extended $L_e = 6h$ upstream and $L_x = 32h$ downstream of the step. The turbulence statistics are independent of z and time t, making the configuration suitable as a reference for simpler CFD codes. For a geometrically identical flow domain in two dimensions, the present study will explore how different levels of turbulence modelling tackle the effect of system rotation on a massively separated turbulent flow.
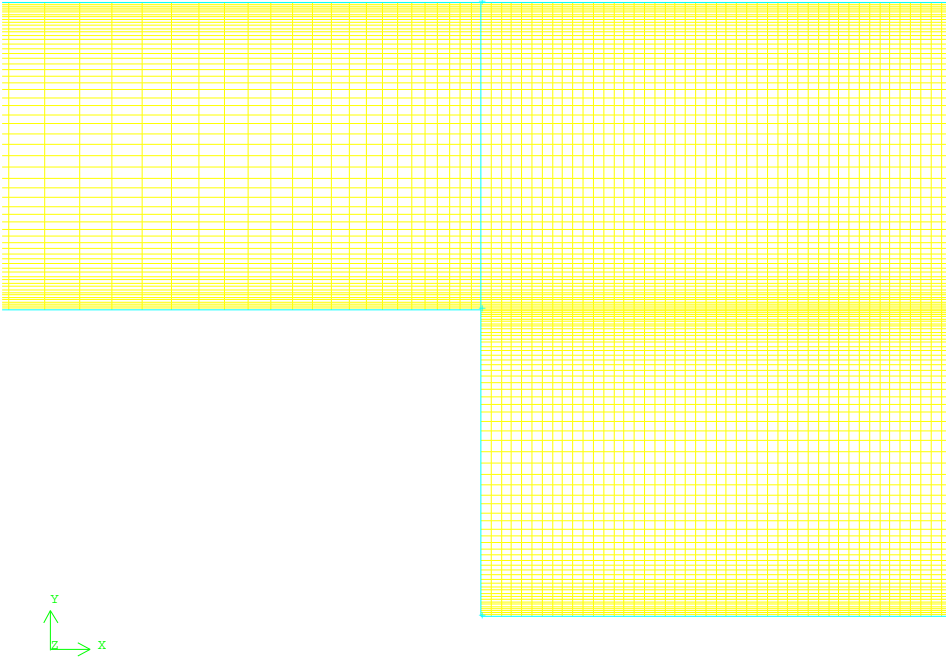
43

Figure 4.2: Segment of the structured BFS grid used in the calculations.

4.2   Grid and precursor calculations

A grid study for the BFS was performed in a previous project work by the author [19]. The resulting grid proved to be fine enough to provide a grid-independent RANS result, and is reused in all of the BFS calculations in the present work. ANSYS Gambit 2.4.6 was used when creating the structured, Cartesian grid with a cell count of 53 040. The cells are quadrilateral and the Map meshing scheme was used. In order to resolve the region close to the inlet and expansion, a bi-exponential function is used for streamwise node distribution before the step. In the separation region between the step and $9h$ downstream of the step, the nodes are distributed uniformly in the streamwise direction. Further downstream, in the recovery region, the cells are stretched in the streamwise direction by an exponential function. A detailed view of the grid around the expansion can be seen in figure 4.2.
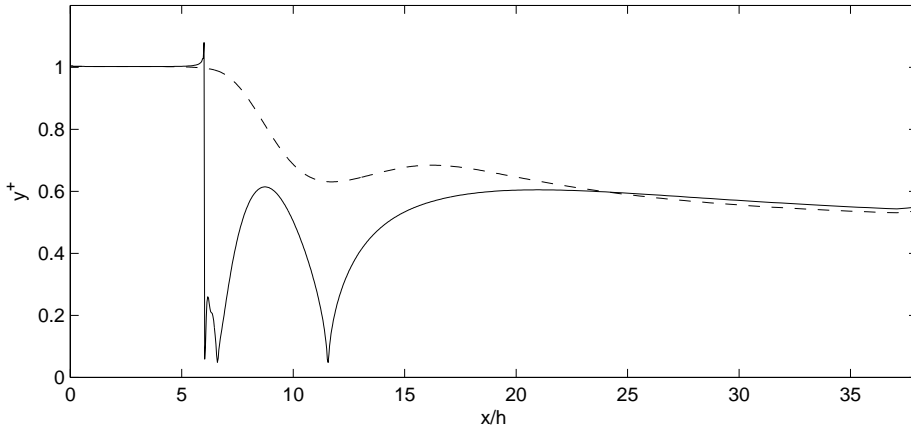
Figure 4.3: Values of y^+ for the grid used in the computations, with a RSM solution. ——, stepped wall; - - -, straight wall.

Upstream of the step, the node interval count is 64 in the x-direction and 60 in the y direction, resulting in a total of 3840 cells. Downstream of the step, the corresponding numbers are 410 node intervals in the x direction and 120 in the y direction. This makes a total of 49 200 cells. A high node density in the wall-normal direction is preferred close to walls and near the shear layer. An identical wall-normal node distribution is applied for all walls parallel to the x direction. The y^+ value at the upper and lower wall is in the order of 1 (figure 4.3) and there is about twenty cells within the viscosity-affected near-wall region. Hence, the boundary layer is well resolved.

Precursor computations were performed in order to ensure a fully developed flow at the inlet of the BFS. One precursor computation was done for each BFS computation. The approach consisted in letting a turbulent flow develop in a channel identical to the inlet channel in the BFS case. The first and second order moments were fully developed after about 60 channel heights downstream of the inlet. The fully developed velocity profile, together with turbulent quantities and stresses, were then applied as inlet conditions in the corresponding BFS case. In all calculations (also the BFS), zero gauge pressure was used at the outlet, together with the no-slip condition at walls.

Chapter 5

Results and discussion

Different classes of turbulence models have been tested for the rotating BFS case in order to explore how they react to system rotation. Since the physical phenomenas in this flow case depend on the rate of system rotation, it will be easier to differentiate between the classes. In the nonrotating case, the turbulence models will encounter challenges when predicting the reattachment length X_r, the correct recovery of the flow and the reattachment process itself. Important rotation-related effects that the models should exhibit are asymmetric fully developed velocity profiles, a correlation between X_r and Ro and the appearance of the separation bubble at the upper wall. All three effects are related to augmentation and dampening of turbulence due to system rotation. Model results will be compared with DNS data from Barri & Andersson [6], making it possible to assess the performance in detail.

There has not been a lot of research focusing on modelling of turbulent flow over a rotating BFS. Nilsen & Andersson [45] used an ASM formulation of the RSM by Launder *et al.* [35], but were hampered by the use of wall functions. The results were however qualitatively good and the the model exhibited a correlation between X_r and Ro consistant with experiments [57], namely that X_r decreases with increasing Ro and vice versa. Agitation and dampening of turbulence was also predicted, but no separation bubble at the straight wall is mentioned in their paper. Later, Pettersson Reif *et al.* [50] validated a quasi-linear v^2–f model and achieved good results.

They were able to predict the correlation between X_r and Ro and found a separation bubble at the straight wall for higher Ro. The results were however not documented in detail. Both studies conclude that the changes in the mean flow field occurring when system rotation is induced, is mainly due to rotational stress production.

In the present study, the commercial CFD software ANSYS Fluent 13.0.0 is used. Fluent has a range of built-in turbulence models, as well as DES and LES formulations. Due to restrictions in computational resources, and since the flow field is statistically homogeneous in the spanwise direction, only two-dimensional computations will be conducted in the present study. As discussed in chapter 3, a RSM is a natural choice for modelling turbulent flows subject to rotation, due to the exact rotational production of Reynolds stresses. RSM computations will thus be emphasised, but also eddy-viscosity models will be tested. Three RSM formulations are included in Fluent. The ω-based RSM did not perform well for the BFS case in [19], and the SSG model [70] is only available with standard wall functions. The *Linear Pressure-Strain Model* was therefore chosen and it is described in section 2.5. The standard k–ε and the Realizable k–ε models of sections 2.4.1 and 2.4.2, respectively, will represent the eddy-viscosity models. The near-wall treatment described in section 2.7.2 is applied in all computations.

The grid and boundary conditions used are described in chapter 4. The Reynolds number, based on the bulk velocity U_b and the step height h, is 5600. Some different rotation numbers will be considered, namely $Ro = 0$, 0.05, 0.1, 0.2 and 0.4. The simulations are performed with a double precision implicit pressure-based coupled solver. By using the pseudo-transient solution method, which is a form of implicit under-relaxation for steady-state cases, convergence was achieved relatively quickly. This solution method uses a pseudo-transient time-stepping approach and has in some cases proven to reduce the required number of iterations by an order of magnitude or more [26]. The PRESTO! discretisation scheme is used for the pressure equation, while the second-order upwind scheme is used for the remaining equations. Iterations were carried out until the sum of the scaled cell residuals for all variables were in the order of 10^{-8} or less.

48

5.1 Streamlines

Streamlines are calculated from the velocities u and v, and yield a general overview of the computational results. Figure 5.1 compares the streamlines obtained with the standard k–ε and the Realizable k–ε models in the nonrotating case and for $Ro = 0.2$. Vertical lines indicate the position downstream of the step. Upstream of the step, the streamlines are parallel, indicating a fully developed mean velocity profile. The flow separates at the step edge and a separation bubble is predicted in all computations. The separation bubble consists of a large clockwise recirculation zone, as well as a small counter-clockwise recirculation zone adjacent to the step corner. It is further seen that the shear layer curves downwards and the flow reattaches at some length downstream of the step. Far downstream the streamlines get more parallel as the velocity profile redevelops.

Comparing figures 5.1a and 5.1b, the standard k–ε model shows essentially the same streamlines for both $Ro = 0$ and $Ro = 0.2$. The k–ε model is a linear eddy-viscosity model which is incapable of predicting Coriolis-force effects on the turbulence field. Since all rotationally induced changes to the velocity field are attributed to changes in the turbulence field, the outcome was not a surprise. A pressure gradient $\partial P_{\text{eff}}/\partial y$ which balances the Coriolis force is predicted by the model, but it will not affect the mean velocity in this confined flow.

The Realizable k–ε model, on the other hand, is a quasi-linear model. Figures 5.1c and 5.1d show a correct correlation between the reattachment length X_r and the rotation number Ro. This is due to the model's eddy-viscosity formulation where C_μ (eq. (2.27)) is a function of rate of rotation and system rotation. The eddy viscosity increases drastically in the shear layer when rotation is induced, causing earlier reattachment. The model is however unable to alter the turbulence field upstream of the step, confirmed by an examination of the turbulent quantities. Turbulence augmentation near the anti-cyclonic wall, and dampening near the cyclonic wall, would lead to high and low values of k, respectively. The computed values of k (not shown herein) are however symmetric about the channel centreline. The region just downstream of the step edge is therefore not as turbulent as it should be, causing less mixing and thus an overpredicted reattachment length compared to DNS data. Note that this also implies a symmetric inlet
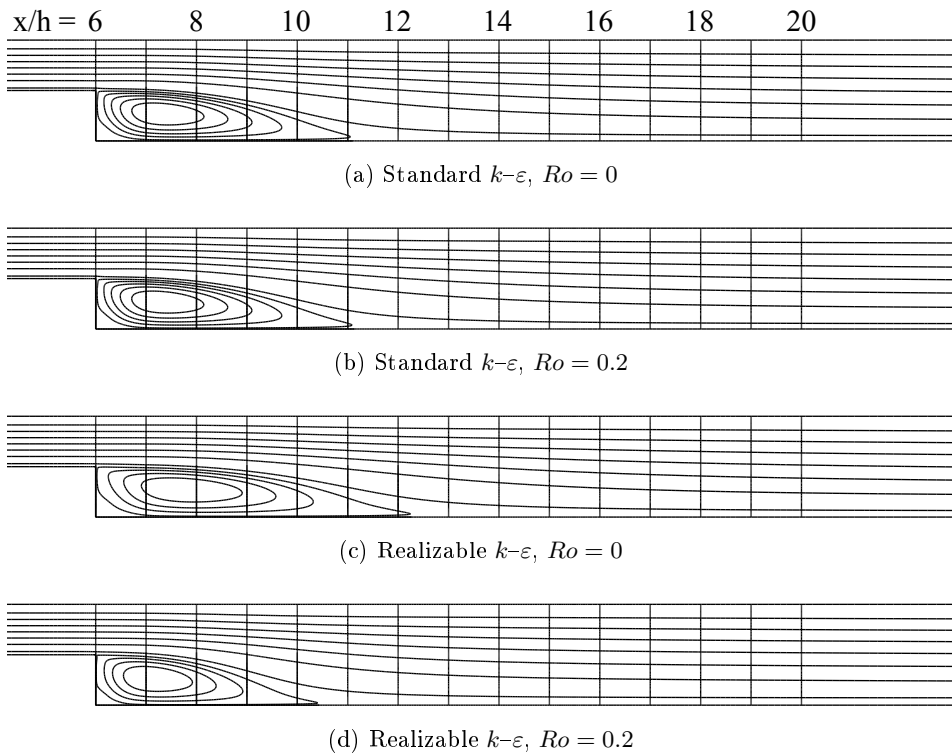
(a) Standard k–ε, $Ro = 0$

(b) Standard k–ε, $Ro = 0.2$

(c) Realizable k–ε, $Ro = 0$

(d) Realizable k–ε, $Ro = 0.2$

Figure 5.1: Streamlines for different computations with k–ε models.

velocity profile, which is the case for both k–ε models.

Figure 5.2 shows the streamlines computed for different rotation numbers by the RSM. The shear layer in the nonrotating case becomes steep near the stepped wall, resulting in a somewhat small recirculation bubble. As system rotation is induced, streamlines on the cyclonic side start to bend downstream of the step, and a separation bubble appears somewhere between $Ro = 0.05$ and $Ro = 0.1$. Within the separation bubble, the flow is recirculating in a counter-clockwise manner. At the same time, the separation bubble at the anti-cyclonic side is reduced in size with increasing Ro. For higher rotation numbers, we see that the separation bubble on the cyclonic side increases dramatically in size, while the other separation bubble gets even smaller. The formation and enlargement of the separation bubble at the straight wall is clearly related to system rotation. Due to
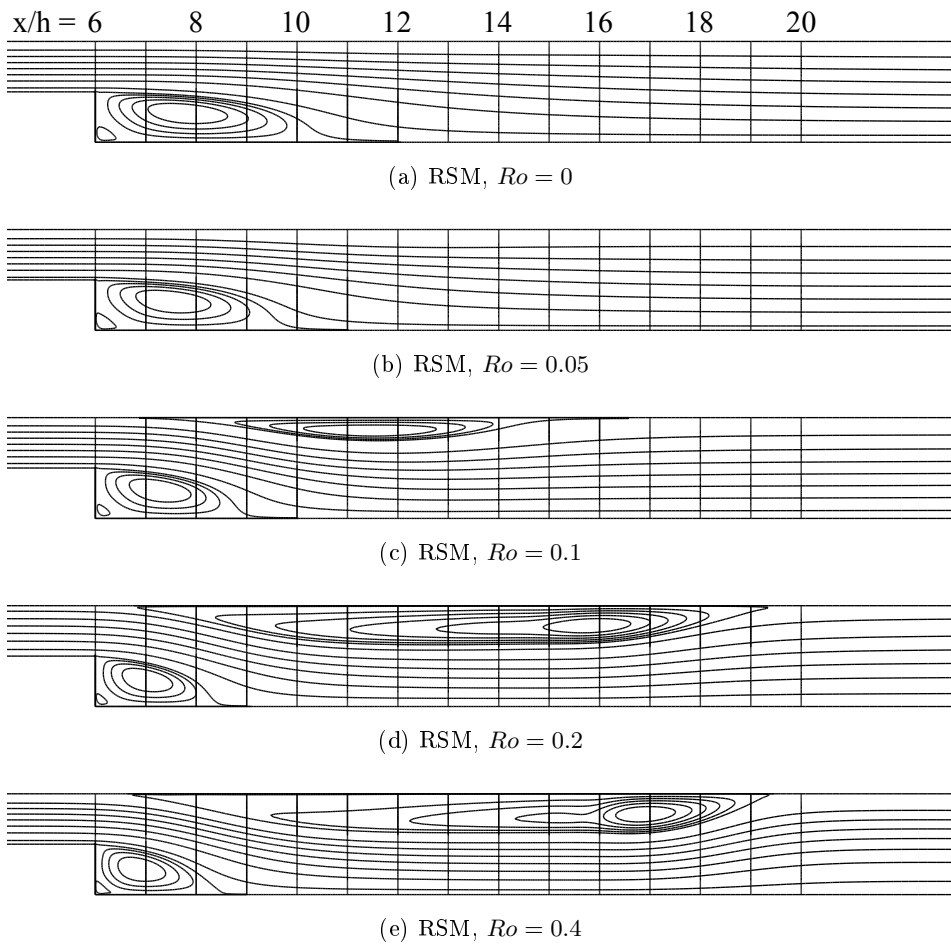
x/h = 6   8   10   12   14   16   18   20

(a) RSM, $Ro = 0$

(b) RSM, $Ro = 0.05$

(c) RSM, $Ro = 0.1$

(d) RSM, $Ro = 0.2$

(e) RSM, $Ro = 0.4$

Figure 5.2: Streamlines for different computations with the Reynolds stress model.

51

the sudden expansion, there will be an adverse pressure gradient near the straight wall (see e.g. [6], [19]), but the channel flow will not separate in the nonrotating turbulent case. When system rotation is induced however, the cyclonic flow near the straight wall becomes less turbulent due to stabilising effects. Analogous to laminar and transitional BFS flow, separation due to the adverse pressure gradient will now become more likely.

By comparing figures 5.2d and 5.2e, it seems that the size of the separation bubbles tends towards a certain value for higher Ro. This seems reasonable, at least for the separation bubble at stepped wall which is dependent on the step geometry. We further observe that between $Ro = 0.1$ and $Ro = 0.2$, the high-velocity region within the recirculating zone at the straight wall shifts towards the downstream part of the zone. The small counter-clockwise recirculation zone adjacent to the step corner is also predicted in all RSM calculations.

5.2   Reattachment length

The separation and reattachment locations can be found by examining the skin friction coefficient $C_f = \tau_{\mathrm{w}}/\frac{1}{2}\rho U_b^2$ at the walls. The computed values for X_r are compared with DNS data in figure 5.3. As seen from the streamlines, the standard k–ε model predicts the same reattachment length independently of Ro, while the Realizable k–ε model yields a shorter length when system rotation is induced. Note that for the latter model, $X_r = 7.8h$ is equal to the DNS data for $Ro = 0$. It is however overpredicted for $Ro = 0.2$, as discussed in the previous section.

For X_r computed with the RSM, a very good correlation with DNS data can be seen for $Ro \geq 0.05$. The predicted reattachment length for $Ro = 0.4$ is merely $0.2h$ shorter than what is found in Barri & Andersson [6]. In Gundersen [19], the author pointed out that the RSM model may have predicted a short reattachment length in the nonrotating case due to inlet conditions that were not fully developed. In the present work, the inlet conditions are fully developed, but the reattachment length $X_r = 5.6h$ did not increase more than $0.1h$, compared to [19]. The influence of the inlet conditions is seemingly not that great in this case, and the defect is presumably found in the model itself.
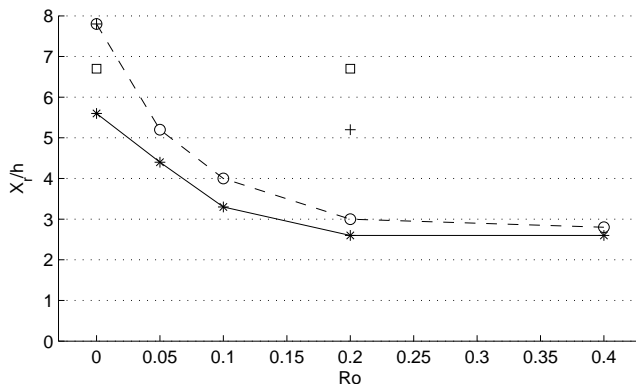
Figure 5.3: Reattachment length at stepped wall for the different computations, based on skin friction coefficient C_f. Symbols: $\square$, standard k–ε; +, Realizable k–ε. Lines: —∗—, RSM; - - -∘- - -, DNS data from Barri & Andersson [6].

5.3 Skin friction coefficient

By examining the skin friction coefficient along the stepped and straight wall, we can get a more detailed impression of the BFS flow. The variation of C_f downstream of the step for the k–ε computations is shown in figure 5.4. A negative C_f denotes backflow near the wall. Both models overpredict the backflow velocity in the nonrotating case, indicated by the minimum value along the stepped wall. The small secondary recirculation zone in the step corner can also be seen, but it is too small compared to the nonrotating DNS results. It can further be seen that the velocity profile is still redeveloping far downstream (the C_f values do not coincide), contrary to the DNS where the velocity profile is essentially fully developed, Barri *et al.* [7].

Notice that the C_f computed by the standard k–ε model is identical for both rotation numbers. For the Realizable k–ε model, the solution shifts somewhat due to system rotation, but figure 5.4b confirms that no separation occurs along the straight wall. The size of the small secondary recirculation zone, as well as the backflow intensity in the large recirculation zone, is computed quite accurately. Thus, the quasi-linear Realizable k–ε model manages to imitate certain rotation-induced effects, but the
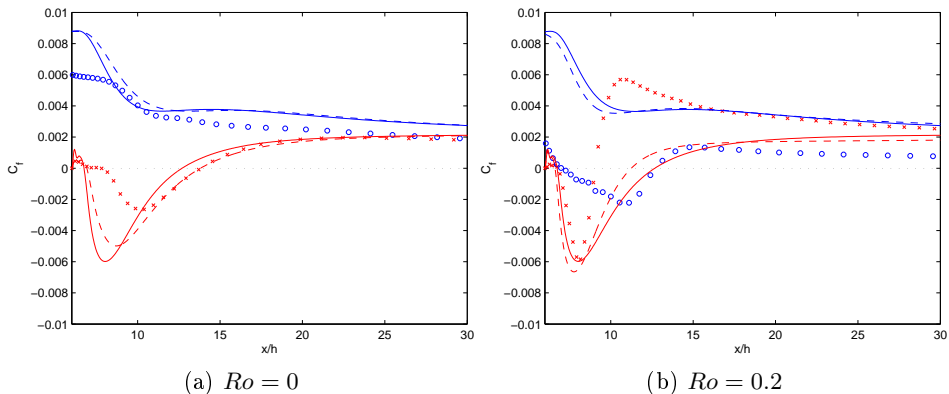
Figure 5.4: Skin friction coefficient C_f for different k–ε computations. Colours: Red, stepped wall; blue, straight wall. Lines: ——, standard k–ε; - - -, Realizable k–ε. Symbols: DNS data from Barri & Andersson [6].

performance is still rather poor due to the absence of stabilising and destabilising effects.

The variation of the skin friction coefficient predicted by the RSM is shown in figure 5.5. In the nonrotating case, the shape and intensity of the large recirculation zone is similar to that from the DNS. The secondary recirculation zone is however too small, leading to premature reattachment. Consistant with the findings in [19], the flow seems to redevelop quickly in the downstream region. When weak system rotation is induced, the calculated values of C_f correspond well with DNS data, as seen in figure 5.5b. Results for the straight wall indicate that the flow actually separates at $x/h \approx 11$, or at least that the flow comes to a standstill. In the downstream redevelopment region, it is seen that C_f is higher at the stepped wall than at the straight wall. This is due to the turbulence augmentation near the stepped wall which occurs for $Ro > 0$. As the flow becomes more turbulent, the velocity gradient becomes steeper, resulting in a higher τ_w. This effect is also seen in the DNS results.

When the rotation number reaches 0.1, seen in figure 5.5c, we immediately recognise the oversized separation bubble at the straight wall, also seen from the streamlines. The length of the bubble, $X_{u2} - X_{u1}$ is about $8.1h$,
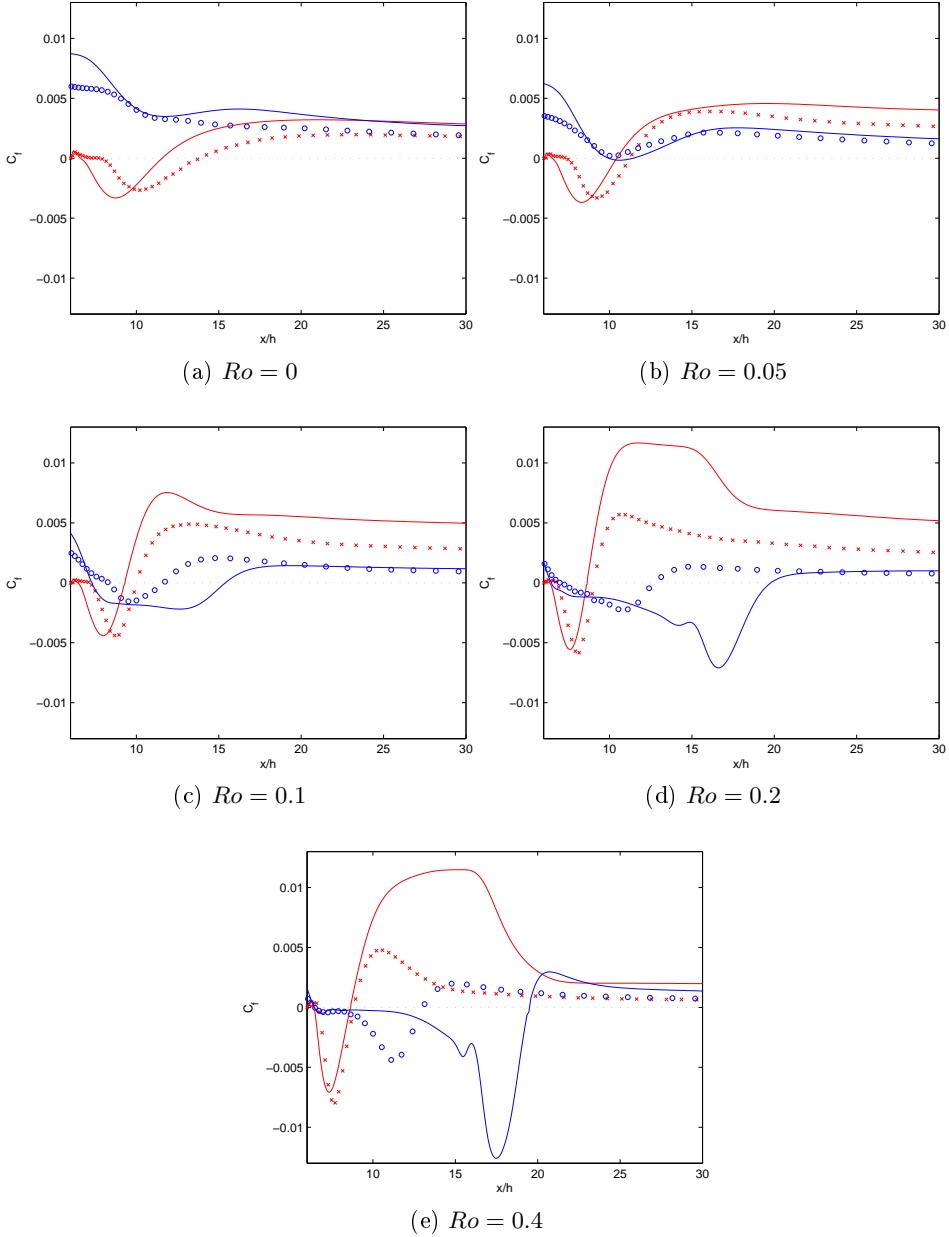
(a) $Ro = 0$

(b) $Ro = 0.05$

(c) $Ro = 0.1$

(d) $Ro = 0.2$

(e) $Ro = 0.4$

Figure 5.5: Skin friction coefficient C_f for the RSM computations. Colours: Red, stepped wall; blue, straight wall. Symbols: DNS data from Barri & Andersson [6].

more than twice the size found in the DNS, which was about $3.3h$. The same tendency is seen for $Ro = 0.2$ and 0.4. The composition of the separation bubble in the high-Ro cases is however similar to the DNS results, with the highest backflow intensity in the downstream part of the bubble. For $Ro = 0.4$, Barri & Andersson [6] noted that a local minimum for C_f appeared along the straight wall, about $1h$ downstream of the step. This indicates the formation of two smaller recirculation zones within the separation bubble, rather than one large. The same phenomenon is indicated by the RSM results, in addition to a more evident local minimum at $x/h \approx 15.5$, caused by the momentum of the intense backflow at $x/h \approx 17.5$.

The backflow intensity is seen to increase with Ro also at the stepped wall. The RSM predicts this separation bubble fairly accurate, although the small secondary recirculation zone is too small. Downstream of reattachment, the model exhibits a global maximum for C_f, related to the separation bubble at the straight wall. As the separation bubble covers about half of the channel in the wall-normal direction, the streamwise velocity between the stepped wall and the bubble must increase in order to uphold mass conservation. The same effect is seen in the DNS results, but the outcome is not so dramatic because of a smaller separation bubble in both x and y direction. The situation is further illustrated by examining the velocity profiles in the next section.

In the downstream redevelopment region, we notice a decrease in C_f at the cyclonic side of the channel, as the rotation number increases. This is due to the stabilising Coriolis-force effect, and consistant with DNS data. For the anti-cyclonic side, C_f increase with increasing Ro up to $Ro = 0.2$. Then, at $Ro = 0.4$, C_f has dropped to a lower value than in the nonrotating case. Accordingly, somewhere between $Ro = 0.2$ and $Ro = 0.4$, $\overline{u'^2}$ becomes smaller than $\overline{v'^2}$, causing the rotational shear stress production term $F_{12}/\rho = -2\Omega(\overline{u'^2} - \overline{v'^2})$ to change sign (see sec. 3.1). Turbulence is thus dampened also at this side of the channel, and the velocity gradient tends towards the one at the straight wall. Note that this applies only to the redeveloping flow downstream of the step. The effective rotation number is higher here than upstream of the step since it depends on the channel height. Being able to predict this effect directly is a good example of the advantages by using a RSM instead of a simpler turbulence model.

56
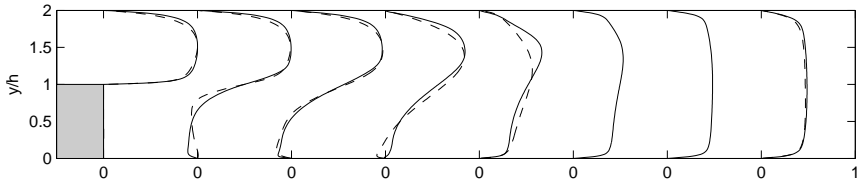
5.4   Velocity profiles

Streamwise velocity profiles $u/U_{\max}$ from the RSM results are shown in figure 5.6. $U_{\max}$ is the maximum inlet velocity in each computation. Velocity profiles are shown for the flow at the step, as well as for seven downstream positions. DNS data from Barri & Andersson [6] is included for comparison, but note that no DNS data is shown for $x/h = 16$ and 20. These two profiles are included due to the oversized separation bubble near the straight wall.

When rotation is induced, the RSM correctly exhibit the characteristic asymmetric velocity profile for the flow over the step. (The velocity profile at the step is somewhat affected by the downstream conditions and is therefore not entirely fully developed.) As Ro increases in parallel shear flow, $U_{\max}$ shifts towards the cyclonic side due to stabilising effects. A region of zero absolute vorticity, where $S = 2\Omega/(\partial v/\partial x - \partial u/\partial y) \approx -1$, appears in the channel core. Zero absolute vorticity signifies that the system vorticity balances the flow vorticity. When v is negligible, the region is characterised by a linear part in the velocity profile with a slope proportional to 2Ω. Overall, the prediction of the fully developed flow at the step is considered fairly good, especially at the anti-cyclonic side of the channel. The computed redeveloping profiles at $x/h = 30$ also correspond well with DNS data, except for $Ro = 0.4$ where the profile is slightly shifted towards the cyclonic side.

The separation bubbles are readily observed by examining the velocity profiles downstream of the step, where $u/U_{\max} < 0$ corresponds to backflow. Predictions for $Ro = 0.05$ are reasonable, but for $Ro \geq 0.01$ we see that the separation bubble along the straight wall extends too far downstream. Additionally, as it expands towards the stepped wall, it blocks the streamwise flow which responds with a higher velocity. The effect is clearly seen for $x/h = 13$ and reflects the overpredicted C_f in figures 5.5d and 5.5e. It seems likely that the overpredicted backflow intensity near the straight wall appears due to the increased velocity near the stepped wall. Velocity profiles for $x/h = 7$, 8 and partly 10 are anyhow rather accurate compared to DNS data. The RSM is evidently struggling with the cyclonic part of the flow, whereas the anti-cyclonic part is well handled.
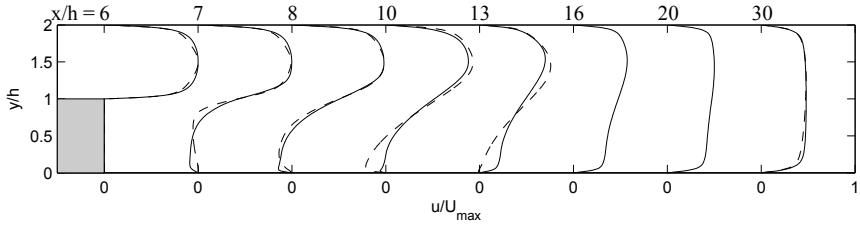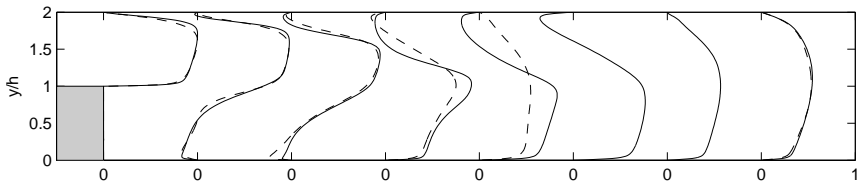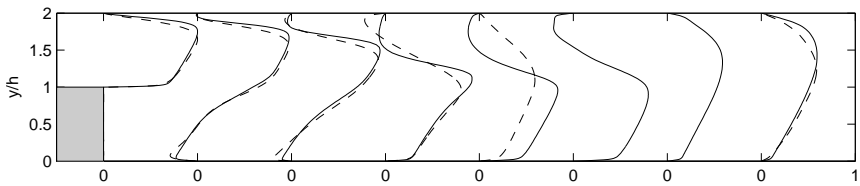
(a) RSM, $Ro = 0$

(b) RSM, $Ro = 0.05$
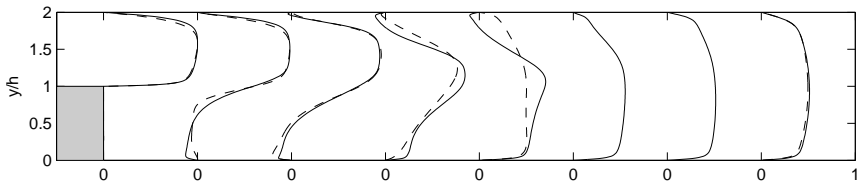
(c) RSM, $Ro = 0.1$

(d) RSM, $Ro = 0.2$

(e) RSM, $Ro = 0.4$

Figure 5.6: Mean streamwise velocity profiles at different locations $x/h = 6$, 7, 8, 10, 13, 16, 20 and 30. ——, RSM; - - -, DNS data, Barri & Andersson [6].

5.5   Reynolds stresses

Reynolds stress contours from the RSM and DNS computations are shown in figure 5.7. Only the case of $Ro = 0.2$ will be considered. Note that the contour values from the RSM and DNS do not correspond, the figure is meant to give a qualitative impression of the stress distribution. Contours near the straight wall in 5.7g and 5.7h represent positive values of $\overline{u'v'}$, while those near the stepped wall are negative.

The predicted distribution of Reynolds stresses at the anti-cyclonic side seems to correspond quite well with the DNS data. Both the curved shear layer and the upstream channel flow is highly turbulent, in correspondence with the production terms in table 4.1. Yet, one exception is seen when comparing the spanwise Reynolds stress $\overline{w'^2}$ in figures 5.7e and 5.7f. The appearance of $\overline{w'^2}$ in the RSM computation is solely due to the redistribution term ϕ_{33}, as the production terms P_{33} and F_{33} are both zero. Barri & Andersson [6] attribute their excessive level of $\overline{w'^2}$ near the wall at $x/h = 9$ to the dynamic flow phenomenon of secondary flows. Longitudinal roll cells were observed in the reattachment zone when inspecting the instantaneous flow field. Rotating in the yz plane, these roll cells will cause high levels of $\overline{w'^2}$, even though the time average of the fluctuations w' naturally vanishes. If the secondary motions are to be resolved, a three-dimensional (or two-dimensional, three-componential) computation is required, so the effect cannot be predicted in the present study.

When it comes to the cyclonic side of the channel, there are more differences. At first sight the contours look quite similar, but the computed values for the wall-normal stresses $\overline{v'^2}$ require further inspection. It is seen from the DNS results in figure 5.7c that rather high values of $\overline{v'^2}$ occur on the cyclonic side for $8 \leq x/h \leq 14$. This tendency is absent in the RSM computation. Values of $\overline{v'^2}$ scaled by the global friction velocity $u_*^2 = -\frac{1}{2\rho}\frac{\partial P_{\text{eff}}}{\partial x}(H-h)$ at $x/h = 10$ are compared with the DNS data in figure 5.8. It is readily seen that the wall-normal stress is considerably underpredicted at the cyclonic side in the RSM computation. High values of wall-normal stress signify more mixing across the shear layer and therefore a suppression the separation bubble at the straight wall. This seems to be the main reason for the prediction of an oversized separation bubble by the RSM.

(a) DNS $\overline{u'^2}$ (b) RSM $\overline{u'^2}$

(c) DNS $\overline{v'^2}$ (d) RSM $\overline{v'^2}$

(e) DNS $\overline{w'^2}$ (f) RSM $\overline{w'^2}$

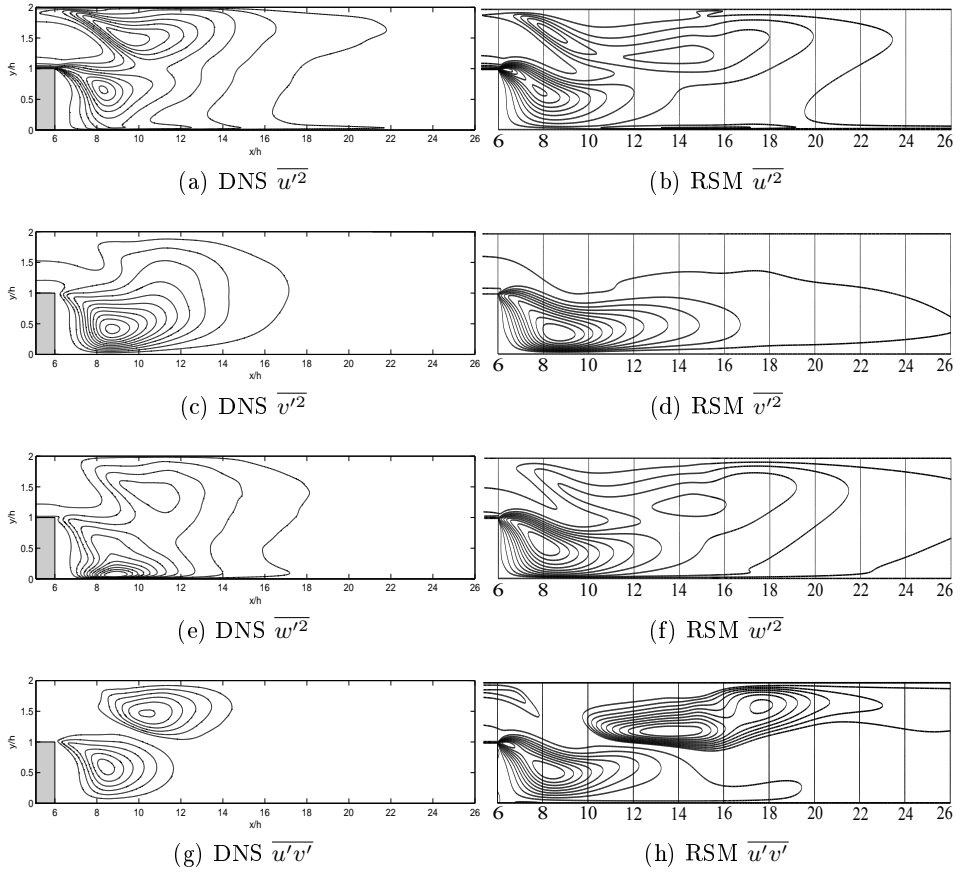(g) DNS $\overline{u'v'}$ (h) RSM $\overline{u'v'}$

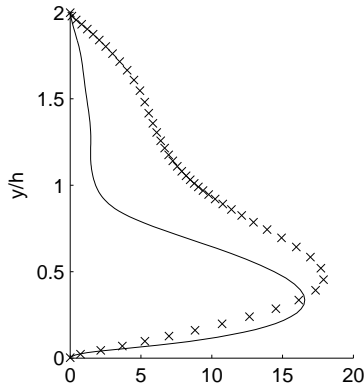Figure 5.7: Reynolds stress contours for $Ro = 0.2$. Left: DNS data from Barri & Andersson [6]. Right: RSM solution.

Figure 5.8: Wall-normal Reynolds stress $\overline{v'^2}/u_*^2$ for $Ro = 0.2$, at $x/h = 10$. DNS data from Barri & Andersson [6] denoted by $\times$.

The high values of $\overline{v'^2}$ predicted by the DNS cannot be attributed to mean shear production P_{22} or rotational production F_{22}. Barri & Andersson [6] show that mean shear production P_{22} is negligible in this region, and F_{22} will act as a sink since $\overline{u'v'}$ is positive. We are then left with the redistribution term ϕ_{ij}. As is normally the case, ϕ_{11} is negative and turbulent energy is distributed to the other diagonal stress components. Contrary to conventional wall-bounded shear flows however, most of the energy from ϕ_{11} is now distributed into wall-normal fluctuations instead of spanwise fluctuations [6]. This is the reason for the high values of wall-normal stress in the cyclonic region. The shear stress $\overline{u'v'}$ is also increased due to an increased $\overline{v'^2}$, as seen in figure 5.7g. It should be noted that the contours in figure 5.7h are somewhat misleading, as shear stress on the cyclonic side is rather low. The highest magnitude on the cyclonic side is only ≈ 0.125 of that at the anti-cyclonic side, whereas as the same ratio in the DNS results is ≈ 0.23.

It seems that the wall-normal redistribution term ϕ_{22} is underpredicted at the cyclonic side in the RSM results. The relatively high values of $\overline{u'^2}$ for $12 \leq x/h \leq 16$ in figure 5.7b may indicate turbulent energy that should have been redistributed into wall-normal fluctuations. Figure 5.7f also indicates that turbulent energy from the streamwise fluctuations in the cyclonic shear layer are redistributed into $\overline{w'^2}$ rather than $\overline{v'^2}$. Hence, the main defect in the RSM calculations, the oversized separation bubble at the cyclonic

61

side of the channel, seems to arise due to a flaw in the modelling of the redistribution term ϕ_{ij}, equation (2.37). This is perhaps not a surprise, as accurate modelling of ϕ_{ij} is regarded as the most difficult part of Reynolds stress equation modelling. The intercoupling between the stresses through production, redistribution, dissipation and diffusion is however an intricate process and an individual inspection of the components in each process is required in order to locate the flaw with certainty.

Chapter 6

Conclusions

A study of how different levels of turbulence modelling tackle the effects of system rotation has been conducted. System rotation gives rise to the fictitious Coriolis and centrifugal forces in the equations of motion, where the Coriolis force significantly affects turbulent flows. Its presence leads to the introduction of a new production term F_{ij} when deriving the transport equations for the Reynolds stresses. The term is dependent on rate of system rotation and will alter the turbulence field accordingly. In shear flows, the general effect is augmentation and dampening of turbulence in regions subjected to anti-cyclonic and cyclonic rotation, respectively. Additionally, system rotation will affect processes such as Reynolds stress redistribution and may induce secondary flows.

An investigation of relevant literature revealed that linear eddy-viscosity turbulence models are unable to predict any Coriolis-force effects on the turbulence field. Such cost efficient models are widely used for industrial applications due to their simplicity. This is however also their vulnerable point, as the simple linear eddy-viscosity formulation relies on the frame-indifferent strain-rate tensor to predict the turbulent stresses. It is however possible to capture rotational effects on the flow field by sensitising the models. This is often done by introducing the rate-of-rotation tensor and the system rotation in the eddy-viscosity formulation. However, the model still exhibits isotropic turbulence which is in strong violation with rotating turbulent flows. Fully nonlinear eddy-viscosity models are able to predict

turbulence anisotropy, but will in any case lack a transport mechanism for the stresses.

The more costly Reynolds stress equation turbulence model class stands out as the natural choice when selecting a RANS turbulence model for rotating flows. This is due to the Reynolds stress production terms and the redistribution term appearing in the Reynolds stress transport equation (2.30). The production terms are exact, meaning that Coriolis-force effects will be predicted to a large extent, independently of the model formulation. Modelling the redistribution process is considered as the main challenge in RSMs and is principally what differentiates the several formulations in the literature.

The use of eddy-resolving simulations has increased considerably during the last decade. The main advantage of LES compared to the RANS approach, is that the effects of rotation are captured directly by solving the filtered Navier–Stokes equations (2.56). As numerical dissipation and limitations of the SGS model are the only sources of incorrectness in LES, the computed results can be very accurate and detailed. A very fine grid and short time step is however required, making LES very costly compared to RANS. A compromise between the two approaches has been made in the DES formulation, where RANS and LES are used near walls and in the free stream, respectively. The DES formulation has proven to yield accurate results for rotating flows at a relatively low cost [75].

Two-dimensional RANS calculations of the turbulent flow over a spanwise rotating backward-facing step were performed with the commercial CFD software ANSYS Fluent. Results were compared with DNS data from Barri & Andersson [6] which corresponded well with the experiments of Rothe & Johnston [57]. As a linear eddy-viscosity model, the standard k–ε model did not manage to predict any effect on the mean velocity field due to system rotation. The solution was essentially the same in both the nonrotating case and for $Ro = 0.2$. The quasi-linear Realizable k–ε model exhibited a correct correlation between the reattachment length X_r and system rotation, although X_r was still overpredicted in the rotating case. No effects on the turbulence field upstream of the step were seen. The quasi-linear eddy-viscosity formulation did only respond to rotation in regions with streamline curvature, e.g. just downstream of the step. The absence of a separation bubble near the straight wall, as well as the overpredicted

reattachment length, can be attributed to this defect.

Except for any secondary flows, the RSM captured all of the rotationally induced effects on the mean flow field seen in Barri & Andersson [6]. In general, the anti-cyclonic part of the flow was predicted accurately. The deviation in reattachment length at the stepped wall for $Ro = 0.4$ was just $0.2h$. At the cyclonic side of the channel, separation occurred at approximately the same rotation rate as in the DNS. For higher rotation rates, the size of the separation bubble is however severely overpredicted in both x and y direction.

Reynolds stress predictions by the RSM compare fairly well with the DNS data. Values of wall-normal stresses at the cyclonic side downstream of the step are however too low. Barri & Andersson [6] attributed their high levels of $\overline{v'^2}$ to the redistribution process. Contrary to conventional wall-bounded shear flows, most of the energy was redistributed into wall-normal, rather than spanwise fluctuations, causing a suppression of the separation bubble. As the Reynolds stress production terms are exact, the oversized separation bubble in the RSM results is attributed to a flaw in the modelling of the redistribution process.

On basis on the present computations, we may conclude that the RSM class is the best choice for two-dimensional calculations of rotating turbulent flows. Although it is crucial to compare results with experimental or DNS data, a RSM will seemingly exhibit the rotationally induced effects on the mean flow field. Still, the present RSM clearly has its limitations, calling for a detailed examination of the individual Reynolds stress transport processes. Model modifications and further validation is then possible. It would also be interesting to assess the performance of the computationally cheaper v^2–f formulation by Pettersson Reif *et al.* [50] in detail. For three-dimensional calculations of rotating flows, further comparison of DES and RANS results would be useful for the community.

Bibliography

[1] H. I. Andersson. Effect of system rotation on free shear flows. *Effect of System Rotation on Turbulence with Applications to Turbomachinery*, September 20 – 23, 2010. VKI Lecture Series.

[2] H. I. Andersson. Introduction to the effects of rotation on turbulence. *Effect of System Rotation on Turbulence with Applications to Turbomachinery*, September 20 – 23, 2010. VKI Lecture Series.

[3] ANSYS Inc. ANSYS 13.0 Help, 2010.

[4] E. Balaras, C. Benocci, and U. Piomelli. Two-layer approximate boundary conditions for large-eddy simulations. *AIAA Journal*, 34:1111–1119, 1996.

[5] J. E. Bardina, P. G. Huang, and T. J. Coakley. Turbulence modeling validation, testing, and development. *AIAA Paper 97-2121*, 1997.

[6] M. Barri and H. I. Andersson. Turbulent flow over a backward-facing step. Part 1. Effects of anti-cyclonic system rotation. *Journal of Fluid Mechanics*, 665:382–417, 2010.

[7] M. Barri, G. K. El Khoury, H. I. Andersson, and B. Pettersen. DNS of backward-facing step flow with fully turbulent inflow. *International Journal for Numerical Methods in Fluids*, 64:777–792, 2009.

[8] H. C. Chen and V. C. Patel. Near-wall turbulence models for complex flows including separation. *AIAA Journal*, 26:641–648, 1988.

[9] T. J. Craft, B. E. Launder, and K. Suga. Development and application of a cubic eddy-viscosity model of turbulence. *International Journal of Heat and Fluid Flow*, 17:108–115, 1996.

[10] B. J. Daly and F. H. Harlow. Transport equations in turbulence. *Physics of Fluids*, 13:2634–2649, 1970.

[11] J. W. Deardorff. A numerical study of three-dimensional turbulent channel flow at large reynolds numbers. *Journal of Fluid Mechanics*, 41:453–480, 1970.

[12] P. A. Durbin. Near-wall turbulence closure modeling without "damping functions". *Theoretical and Computational Fluid Dynamics*, 3:1–13, 1991.

[13] P. A. Durbin. A Reynolds stress model for near-wall turbulence. *Journal of Fluid Mechanics*, 249:465–498, 1993.

[14] P. A. Durbin and B. A. Pettersson Reif. On Algebraic Second Moment Models. *Flow, turbulence and combustion*, 63:23–37, 2000.

[15] P. A. Durbin and B. A. Pettersson Reif. *Statistical Theory and Modeling for Turbulent Flows*. John Wiley & Sons, Ltd., second edition, 2011.

[16] M. Germano, U. Piomelli, P. Moin, and W. H. Cabot. A dynamic subgrid-scale eddy viscosity model. *Physics of Fluids A: Fluid Dynamics*, 3:1760–1765, 1991.

[17] M. M. Gibson and B. E. Launder. Ground effects on pressure fluctuations in the atmospheric boundary layer. *Journal of Fluid Mechanics*, 86:491–511, 1978.

[18] F. F. Grinstein, L. G. Margolin, and W. Rider. *Implicit large eddy simulation: Computing turbulent fluid dynamics*. Cambridge University Press, 2007.

[19] T. Ø. K. Gundersen. Numerical simulation of separated turbulent flow. Project work, Norwegian University of Science and Technology, December 2010.

[20] K. Hanjalić and S. Jakirlić. Second-moment turbulence closure modelling. In *Closure strategies for turbulent and transitional flows*, pages 47–101. Cambridge University Press, 2002.

[21] A. Hellsten and S. Wallin. Explicit algebraic Reynolds stress and non-linear eddy-viscosity models. *International Journal of Computational Fluid Dynamics*, 23:349–361, 2009.

[22] J. C. R. Hunt and J. M. R. Graham. Free-stream turbulence near plane boundaries. *Journal of Fluid Mechanics*, 84:209–235, 1978.

[23] G. Iaccarino, A. Ooi, P. A. Durbin, and M. Behnia. Reynolds averaged simulation of unsteady separated flow. *International Journal of Heat and Fluid Flow*, 24:147–156, 2003.

[24] S. Jakirlić, C. Tropea, and K. Hanjalić. Computations of rotating channel flows with a low-Re-number second-moment closure model, 7th ERCOFTAC. In *IAHR Workshop on Refined Flow Modelling UMIST, Manchester*, pages 28–29, 1998.

[25] W. P. Jones and B. E. Launder. The prediction of laminarization with a two-equation model of turbulence. *International Journal of Heat and Mass Transfer*, 15:301–314, 1972.

[26] M. Keating. Accelerating CFD Solutions. *ANSYS Advantage*, 5:48–49, 2011.

[27] R. Kristoffersen and H. I. Andersson. Direct simulations of low-Reynolds-number turbulent flow in a rotating channel. *Journal of Fluid Mechanics*, 256:163–197, 1993.

[28] R. Kristoffersen, P. J. Nilsen, and H. I. Andersson. Validation of Reynolds stress closures for rotating channel flows by means of direct numerical simulations. *Engineering Turbulence Modelling and Experiments*, pages 145–152, 1990.

[29] P. K. Kundu and I. M. Cohen. *Fluid Mechanics*. Academic Press, fourth edition, 2008.

[30] B. E. Launder. Second-moment closure: Present... and future? *International Journal of Heat and Fluid Flow*, 10:282–300, 1989.

[31] B. E. Launder, G. J. Reece, and W. Rodi. Progress in the Development of a Reynolds-Stress Turbulence Closure. *Journal of Fluid Mechanics*, 3:537–566, 1975.

[32] B. E. Launder and N. Shima. Second-moment closure for the near-wall sublayer: Development and application. *AIAA Journal*, 27:1319–1325, 1989.

[33] B. E. Launder and D. B. Spalding. Lectures in mathematical models of turbulence. 1972.

[34] B. E. Launder and D. P. Tselepidakis. Application of a new second-moment closure to turbulent channel flow rotating in orthogonal mode. *International Journal of Heat and Fluid Flow*, 15:2–10, 1994.

[35] B. E. Launder, D. P. Tselepidakis, and B. A. Younis. A second-moment closure study of rotating channel flow. *Journal of Fluid Mechanics*, 183:63–75, 1987.

[36] D. C. Leslie and G. L. Quarini. The application of turbulence theory to the formulation of subgrid modelling procedures. *Journal of Fluid Mechanics*, 91:65–91, 1979.

[37] F. S. Lien and M. A. Leschziner. Assessment of turbulence-transport models including non-linear RNG eddy-viscosity formulation and second-moment closure for flow over a backward-facing step. *Computers & fluids*, 23:983–1004, 1994.

[38] D. K. Lilly. The representation of small scale turbulence in numerical simulation experiments. In *IBM Scientific Computing Symposium on Environmental Sciences*, pages 195–210, 1967.

[39] D. K. Lilly. A proposed modification of the germano subgrid-scale closure method. *Physics of Fluids A: Fluid Dynamics*, 4:633–635, 1992.

[40] L. Marstorp, G. Brethouwer, O. Grundestam, and A. Johansson. Explicit algebraic subgrid stress models with application to rotating channel flow. *Journal of Fluid Mechanics*, 639:403–432, 2009.

[41] F. R. Menter. Two-equation eddy-viscosity turbulence models for engineering applications. *AIAA Journal*, 32:1598–1605, 1994.

[42] F. R. Menter. Review of the shear-stress transport turbulence model experience from an industrial perspective. *International Journal of Computational Fluid Dynamics*, 23:305–316, 2009.

[43] F. R. Menter and Y. Egorov. The scale-adaptive simulation method for unsteady turbulent flow predictions. Part 1: Theory and model description. *Flow Turbulence and Combustion*, 85:113–138, 2010.

[44] F. R. Menter, M. Kuntz, and R. Langtry. Ten years of industrial experience with the SST turbulence model. *Turbulence, heat and mass transfer*, 4:625–632, 2003.

[45] P. J. Nilsen and H. I. Andersson. Rotational effects on sudden-expansion flows. *Engineering Turbulence Modelling and Experiments*, pages 65–72, 1990.

[46] M. Oberlack, W. Cabot, B. A. Petterson Reif, and T. Weller. Group analysis, direct numerical simulation and modelling of a turbulent channel flow with streamwise rotation. *Journal of Fluid Mechanics*, 562:383–403, 2006.

[47] V. C. Patel, W. Rodi, and G. Scheuerer. Turbulence models for near-wall and low Reynolds number flows: A review. *AIAA journal*, 23:1308–1319, 1985.

[48] B. A. Pettersson and H. I. Andersson. Near-wall Reynolds-stress modelling in noninertial frames of reference. *Fluid Dynamics Research*, 19:251–276, 1997.

[49] B. A. Pettersson Reif. Towards a nonlinear eddy-viscosity model based on elliptic relaxation. *Flow, turbulence and combustion*, 76:241–256, 2006.

[50] B. A. Pettersson Reif, P. A. Durbin, and A. Ooi. Modeling rotational effects in eddy-viscosity closures. *International journal of heat and fluid flow*, 20:563–573, 1999.

[51] B. A. Pettersson Reif, M. Mortensen, and C. A. Langer. Towards Sensitizing the Nonlinear v^2-f Model to Turbulence Structures. *Flow, Turbulence and Combustion*, 83:185–203, 2009.

[52] U. Piomelli. Wall-layer models for large-eddy simulations. *Progress in Aerospace Sciences*, 44:437–446, 2008.

[53] S. B. Pope. A more general effective-viscosity hypothesis. *Journal of Fluid Mechanics*, 72:331–340, 1975.

[54] A. Raufeisen, M. Breuer, T. Botsch, and A. Delgado. LES validation of turbulent rotating buoyancy-and surface tension-driven flow against DNS. *Computers & Fluids*, 38:1549–1565, 2009.

[55] J. R. Ristorcelli, J. L. Lumley, and R. Abid. A rapid-pressure covariance representation consistent with the Taylor–Proudman theorem materially frame indifferent in the two-dimensional limit. *Journal of Fluid Mechanics*, 292:111–152, 1995.

[56] W. Rodi. A new algebraic relation for calculating the reynolds stresses. In *Gesellschaft Angewandte Mathematik und Mechanik Workshop Paris France*, volume 56, page 219, 1976.

[57] P. H. Rothe and J. P. Johnston. Free shear layer behavior in rotating systems. In *Turbulent Boundary Layers: Forced, Incompressible, Non-Reacting*, volume 1, pages 23–26, 1979.

[58] J. Rotta. Statistische theorie nichthomogener turbulenz. *Zeitschrift für Physik*, 129:547–572, 1951.

[59] T.-H. Shih, W. W. Liou, A. Shabbir, Z. Yang, and J. Zhu. A new k–ε eddy viscosity model for high reynolds number turbulent flows. *Computers & Fluids*, 24:227–238, 1995.

[60] N. Shima and H. Kobayashi. Modelling of the Reynolds stress redistribution with a wall effect vector. *Fluid dynamics research*, 39:320–333, 2007.

[61] Y. Shimomura. Turbulence modeling suggested by system rotation. *Near-wall turbulent flows*, pages 115–123, 1993.

[62] M. Shur, P. R. Spalart, K. D. Squires, M. Strelets, and A. Travin. Three dimensionality in Reynolds-averaged Navier-Stokes solutions around two-dimensional geometries. *AIAA journal*, 43:1230–1242, 2005.

[63] J. Smagorinsky. General circulation experiments with the primitive equations. *Monthly weather review*, 91:99–164, 1963.

[64] P. E. Smirnov and F. R. Menter. Sensitization of the SST Turbulence Model to Rotation and Curvature by Applying the Spalart–Shur Correction Term. *Journal of Turbomachinery*, 131:041010, 2009.

[65] P. Spalart. Detached-eddy simulation. *Annual Review of Fluid Mechanics*, 41:181–202, 2009.

[66] P. R. Spalart. Direct simulation of a turbulent boundary layer up to $R_\theta = 1410$. *Journal of Fluid Mechanics*, 187:61–98, 1988.

[67] P. R. Spalart and S. R. Allmaras. A one-equation turbulence model for aerodynamic flows. aiaa paper 92-0439. In *30th AIAA Aerospace Sciences Meeting, Reno, USA*, 1992.

[68] P. R. Spalart and M. Shur. On the sensitization of turbulence models to rotation and curvature. *Aerospace Science and Technology*, 1:297–302, 1997.

[69] C. G. Speziale. Turbulence Modeling in Noninertial Frames of Reference. *Theoretical and Computational Fluid Dynamics*, 1:3–19, 1989.

[70] C. G. Speziale, S. Sarkar, and T. B. Gatski. Modelling the pressure-strain correlation of turbulence: An invariant dynamical systems approach. *Journal of Fluid Mechanics*, 227:245–272, 1991.

[71] C. G. Speziale and S. Thangam. Numerical study of secondary flows and roll-cell instabilities in rotating channel flow. *Journal of Fluid Mechanics*, 130:377–395, 1983.

[72] H. M. Stommel and D. Moore. *An introduction to the Coriolis force*. Columbia University Press, 1989.

[73] M. Strelets. Detached eddy simulation of massively separated flows. In *AIAA, Aerospace Sciences Meeting and Exhibit, 39th, Reno, NV*, 2001.

[74] H. K. Versteeg and W. Malalasekera. *An Introduction to Computational Fluid Dynamics – The Finite Volume Method*. Pearson Education Limited, 2 edition, 2007.

[75] A. K. Viswanathan and D. K. Tafti. Detached eddy simulation of flow and heat transfer in fully developed rotating internal cooling channel with normal ribs. *International journal of heat and fluid flow*, 27:351–370, 2006.

[76] B. C. Wang and D. J. Bergstrom. A dynamic nonlinear subgrid-scale stress model. *Physics of Fluids*, 17:035109, 2005.

[77] D. C. Wilcox. *Turbulence Modelig for CFD*. DCW Industries Inc., La Cañada, California, 2 edition, 2004.

[78] Q. Q. Xun, B. C. Wang, and E. Yee. Large-eddy simulation of turbulent heat convection in a spanwise rotating channel flow. *International Journal of Heat and Mass Transfer*, 54:698–716, 2011.